

MELTING PRESSURE THERMOMETRY AND
MAGNETICALLY ORDERED SOLID ^3He

BY

WENHAI NI

A DISSERTATION PRESENTED TO THE GRADUATE SCHOOL
OF THE UNIVERSITY OF FLORIDA IN PARTIAL FULFILLMENT
OF THE REQUIREMENTS FOR THE DEGREE OF
DOCTOR OF PHILOSOPHY

UNIVERSITY OF FLORIDA

1994

ACKNOWLEDGMENTS

I would like to express my sincere gratitude to my research advisor E. Dwight Adams, for his guidance and encouragement throughout my graduate student career and for the opportunity to work in this fascinating low temperature physics. Without his help and encouragement, this work would have been impossible. During these years, I was also greatly influenced by his humor, enthusiasm and expertise in various experiments.

My gratitude also goes to professors Gary Ihas, Mark Meisel, Neil Sullivan for teaching me the basic techniques used in the low temperature physics. I especially benefited from the conversations and discussions with Yasumasa Takano during the course of this work; he helped me to understand the related physics in low temperature experiments.

Very special thanks is given to Dr. Jian-Sheng Xia, who taught me all kinds of tricky experimental techniques after I chose to do research in low temperature physics. He collaborated with me during the course of this work. As optimistic as he always had been, his encouragement was very special when the experiment did not go well.

I would also like to thank those engineers in the machine shop and in the electronic shop. Without their expertise and help this work would not have been possible. I am especially indebted to Gregory Labbe and Brian Lothrop in the cryogenic shop, who continuously supplied liquid helium during several months' running of the experiments.

I thank Tien Lang and Paul Moyland for their unselfish help and friendship, especially during those days when we worked together in the MicroKelvin Laboratory.

I am thankful to Professor Henri Van Rinsvelt for his help during the early stage of the ^{60}Co gamma ray radiation measurements, and to Professors Christopher Stanton and Kermit Sigmon for serving on my dissertation committee. I am grateful to Drs. Penny Haskins and Jack McKisson of Institute for Space Science and Technology (ISST) for lending me the germanium detector and the computer-based multichannel analyzer for the ^3He melting pressure thermometry experiment.

I would also like to thank the family of Carmen Campos in Puerto Rico for their love and friendship.

Finally I would like to thank my own family in China, who have sacrificed immensely to support my education and have shown their love and care.

This work was supported by the National Science Foundation, Low Temperature Physics, Grant No. DMR-9019736.

TABLE OF CONTENTS

	<u>Page</u>
ACKNOWLEDGMENTS.....	ii
TABLE OF CONTENTS.....	iv
LIST OF TABLES.....	vi
LIST OF FIGURES.....	vii
ABSTRACT.....	ix
CHAPTERS	
I. INTRODUCTION.....	1
³ He Melting Pressure Thermometry.....	1
Nuclear Magnetism in Solid ³ He.....	5
Magnetic Order in Solid ³ He.....	5
Thermodynamic Experimental Results.....	7
Microscopic Measurements.....	9
Review of Theory.....	10
II. EXPERIMENTAL TECHNIQUES.....	19
Introduction.....	19
Crysotat.....	19
³ He Melting Pressure Thermometer.....	26
³ He Melting Pressure Cell Design.....	26
³ He Melting Pressure Cell Calibration and Measurement.....	28
Pt NMR Thermometer.....	35
Pt NMR Thermometer Design.....	35
Principle of Pt NMR Thermometer.....	35
Electronics for Pt NMR.....	38
⁶⁰ Co Nuclear Orientation Thermometer.....	42
Measuring Anisotropy and the Determination of Temperature.....	47

Sample Preparation and Thermal Contact.....	47
Tungsten Superconducting Fixed Point Thermometer.....	50
Design of the Tungsten Superconducting Fixed Point Thermometer.....	50
Heating Problem.....	51
Effects of DC Magnetic Field.....	55
III. ^3He MELTING PRESSURE THERMOMETRY EXPERIMENT.....	56
Tungsten Superconducting Transition.....	56
Temperature and Melting Pressure Measurements.....	58
Results and Discussions.....	64
IV. THERMODYNAMICS OF ORDERED SOLID ^3He	75
Introduction.....	75
Magnetic Phase Diagram.....	76
Order of the HFP-PP Transition.....	81
Spin-Wave Velocity in the Ordered Phases.....	88
Entropy and Magnetization.....	93
Solid ^3He Molar Volume at Melting Below 1 mK.....	102
Conclusions.....	109
APPENDIX.....	111
REFERENCES.....	115
BIOGRAPHICAL SKETCH.....	119

LIST OF TABLES

<u>Table</u>		<u>Page</u>
1.	Cobalt NO anisotropy versus temperature.....	44
2.	Pressure difference between fixed points.....	64
3.	Comparison of fixed point among different groups.....	67
4.	Calculated A transition temperature from the melting pressure difference.....	71
5.	Measured B - T coordinates for the magnetic phase diagram.....	77
6.	B - T coordinates for the special points.....	79
7.	γ -ray absorption coefficient.....	111

LIST OF FIGURES

<u>Figure</u>	<u>Page</u>
1.1 Melting curve of ^3He	2
1.2 P - T - B phase diagram of liquid and solid ^3He	6
1.3 Ring exchanges in the bcc lattice.....	15
1.4 Magnetic phase diagram by multiple-exchange theory.....	17
1.5 Calculated magnetization versus temperature.....	18
2.1 Experimental arrangement.....	21
2.2 Cooling power of the dilution refrigerator.....	22
2.3 Demagnetization of the PrNi ₅ nuclear stage.....	24
2.4 Melting pressure cell.....	27
2.5 Electronic diagram for melting pressure cell.....	29
2.6 ^3He gas handling panel.....	31
2.7 Melting pressure cell calibration.....	32
2.8 Pressure difference between the measured points and the fit.....	33
2.9 Principle of Pt NMR thermometry.....	36
2.10 Electronics for measuring the Pt NMR temperature.....	39
2.11 Tuning of the Pt NMR circuit.....	40
2.12 Digitized Pt FID signal.....	41
2.13 γ -ray directional distribution of ^{60}Co	45
2.14 γ -ray anisotropy and its sensitivity.....	46
2.15 Electronics for measuring the γ -ray.....	48
2.16 γ -ray spectrum of ^{60}Co NO thermometer.....	49

2.17	Tungsten superconducting fixed point device.....	52
2.18	Electronic diagram for measuring the tungsten thermometer.....	53
3.1	Measured tungsten superconducting transition.....	57
3.2	Temperature control in taking the γ -ray counts.....	60
3.3	Signatures of fixed points.....	62
3.4	Pt NMR calibration against ^{60}Co NO thermometer.....	65
3.5	Comparison of different temperature scales.....	72
3.6	Melting pressure slope.....	73
4.1	Magnetic phase diagram measured in this work.....	80
4.2	Melting pressure measurement by Tang <i>et al.</i>	83
4.3	Melting pressure versus temperature across the HFP-PP transition.....	85
4.4	Experimental arrangement for $B=0.653$ T.....	86
4.5	Entropy versus temperature at the HFP-PP transition.....	87
4.6	Entropy discontinuity versus field at the HFP-PP transition.....	89
4.7	Magnetic phase diagram B - P	90
4.8	Melting pressure versus T^4	92
4.9	Spin-wave velocity as a function of field.....	94
4.10	Melting pressure versus temperature at various fields.....	95
4.11	Entropy versus temperature for various fields studied.....	97
4.12	Family of entropy versus temperature curves.....	99
4.13	Entropy and magnetization discontinuity across the LFP-PP transition.....	100
4.14	Family of magnetization versus temperature.....	101
4.15	Molar volume minimum near 1 mK.....	103
4.16	Isochoric pressure near melting molar volume.....	107
A1	Geometry of source-detector configuration.....	113
A2	Calculated solid angle corrections.....	114

Abstract of Dissertation presented to the Graduate School
of the University of Florida in Partial Fulfillment of the
Requirements for the Degree of Doctor of Philosophy

MELTING PRESSURE THERMOMETRY AND
MAGNETICALLY ORDERED SOLID ^3He

BY

WENHAI NI

AUGUST, 1994

Chairman: Professor E. Dwight Adams
Major Department: Physics

In this thesis, two separate experiments on solid ^3He are presented. In the first experiment, the ^3He melting pressure has been measured precisely from 500 μK to 25 mK. Temperatures were determined from a ^{60}Co nuclear orientation (NO) primary thermometer and Pt NMR, calibrated against the NO thermometer, as a secondary thermometer. The values for the fixed points on the melting curve are: the superfluid ^3He A transition $T_A = 2.505$ mK, the A-B transition $T_{AB} = 1.948$ mK, and the solid ordering temperature $T_N = 0.934$ mK. The functional form for $P(T)$ relative to the solid ordering transition pressure P_N is provided.

In the second experiment, the melting pressures of ^3He across the various magnetic ordering transitions and in magnetic fields up to 0.65 T have been measured. A precise magnetic phase diagram B - T of solid ^3He is obtained. The transitions from the low field phase (LFP) to the high field phase (HFP) and to the paramagnetic disordered phase (PP) are first order. The phase transition from the HFP to PP is identified as first order

from the triple point of the phase diagram to about 0.65 T, above which it is second order phase. The solid ^3He entropy and the magnetization are determined from the Clausius-Clapeyron equations. In the LFP, the melting pressure is proportional to T^4 up to the phase boundary, with a constant spin wave velocity of about 7.8 cm/s, indicating a roughly temperature-independent magnetization at each field. In the HFP, the melting pressure deviates from the T^4 dependence very near the HFP-PP transition, resulting in a very rapid entropy change. From the analysis of the melting pressure data, a very shallow molar-volume minimum was found at the ordering transition T_N .

CHAPTER I INTRODUCTION

³He Melting Pressure Thermometry

Because of the zero-point motion, weak attractive interaction and light mass of the atoms, ³He remains liquid under its own vapor pressure, even at $T=0$. Liquid ³He can be solidified by the application of pressure. The melting pressure P , where the liquid and solid ³He coexist, is a well defined function of temperature T , which in principle can be derived through the Clausius-Clapeyron equation:

$$\frac{dP}{dT} = \frac{S_s - S_l}{V_s - V_l}, \quad \text{Eq. (1.1)}$$

where S_s and S_l are the entropies of the solid and liquid, respectively, and $\Delta V = V_s - V_l$ is the molar volume change on melting. Figure 1.1 shows the melting curve of ³He. One interesting aspect of the melting curve is that there is a pressure minimum near $T=0.32$ K, where the entropies of the solid and the liquid are equal. Below 0.32 K, the entropy of the liquid is smaller than that of the solid (which remains about $R \ln 2$ above 10 mK), therefore the melting curve has a negative slope. Approaching zero temperature, the liquid undergoes the superfluid A and AB transitions while the solid undergoes the magnetic ordering transition to be discussed later. These transitions create unique signatures along the melting curve which can be very easily detected in experiments. Eventually as $T \rightarrow 0$ both S_s and S_l approach to zero according to the third law of thermodynamics, and the melting curve slope becomes zero.

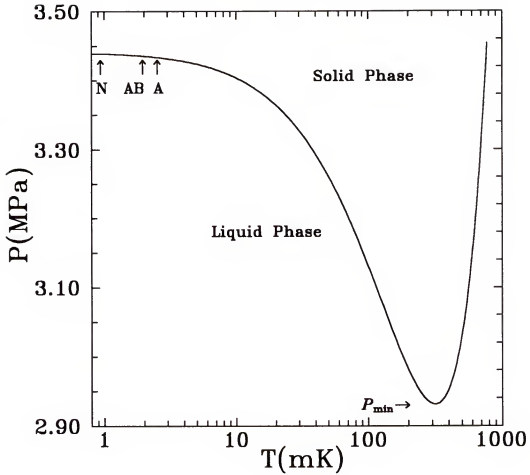


Figure 1.1 Melting curve of ^3He . A, AB and N are the superfluid ^3He A, AB and solid ordering transitions; P_{min} near 0.32 K is the pressure minimum, at which the entropies of the solid and the liquid are equal.

The usefulness of using ^3He melting pressure for thermometry in the milliKelvin temperature range has been recognized for over 20 years [1,2]. The advantages of this thermometry are obvious: 1. the melting pressure can be measured with high resolution, allowing the temperatures to be determined within a few μK ; 2. it provides continuous temperature readings, and the thermal time constant is small; 3. three phase transition points along the melting curve (the superfluid A, AB and the solid ordering transitions) are easy to detect and serve as temperature fixed points, very much like the case of superconductive fixed points, except these three points are the inherit properties of ^3He ; 4. the measurement involves very simple equipment and techniques and with almost no dissipation of heat. In addition, measurements of the latent heat due to liquid-solid conversion can provide the absolute temperature, through the Clausius-Clapeyron equation [3]. ^3He melting pressure thermometry now serves an interim standard and as a convenient means for comparison of results from different laboratories.

However, in order to use the ^3He melting pressure thermometer, a melting pressure versus temperature relationship, P - T , needs to be established. Using the latent heat method mentioned above, Halperin *et al.* [3] made extensive measurements and identified the temperature for superfluid A transition as $T_A=2.75$ mK.

A P - T relationship can be established by using a secondary thermometer, most commonly magnetic thermometers which uses the Curie-Weiss law for interpolating or extrapolating from the known fixed temperature points. Greywall and Busch [4], using a secondary cerium magnesium nitrate (CMN) thermometer calibrated against the NBS fixed points at nominal temperatures of 100, 160, and 200 mK, measured the P - T relationship from 250 mK down to 10 mK. The temperature below 10 mK was provided by the renormalized Halperin scale, which was forced to coincide with NBS-CTS-1983 scale [5] at the superconducting transition of tungsten T_W . In this scale they found $T_A=2.708$ mK.

In Greywall's most recent work [6], the tungsten transition temperature T_W was used to determine one of the parameters for his lanthanum-diluted cerium magnesium nitrate (LCMN) thermometer, which was used to measure the P - T relationship down to the solid ordering temperature. However, in order to determine another parameter, he made the assumption, based on Fermi-liquid theory, that the specific heat of normal liquid ^3He at low temperature is linear in temperature. This scale gave $T_A=2.491$ mK, about 10% lower than the previously accepted value.

Since Greywall's work, Fukuyama *et al.*[7] made independent measurements of $P(T)$ and obtained $T_A=2.48$ mK. Their temperatures were provided by a pulsed platinum NMR thermometer, calibrated against Greywall's scale in the range of 15 to 45 mK.

The need for a temperature scale based on thermodynamics or using a primary standard has long been recognized and was undertaken at the National Institute of Standards and Technology, NIST (previously National Bureau of Standards, NBS) [8]. Their temperatures were determined by a Josephson junction noise thermometer (a primary thermometer), several superconducting fixed points, and a CMN thermometer for interpolation. Above 15 mK, their results were in good agreement with those of Greywall [6]. However, below 15 mK, their temperatures started to read higher than those of Greywall. At 7 mK, the lowest temperature in their measurements, the deviation was 1.6%. If this trend persisted, the temperature at the A transition would be 3.2% greater.

While the work at NIST is of high precision, unfortunately, it does not extend to lower temperatures to include the fixed points on the melting curve mentioned above.

In this work, the melting pressure thermometry for temperatures between 0.5 mK and 25 mK is established. Temperatures were obtained from a ^{60}Co nuclear orientation (NO) primary thermometer and a pulsed platinum NMR secondary thermometer, calibrated against the NO thermometer. It should be emphasized that the melting pressure has enough sensitivity for thermometry to well below the solid ordering temperature T_N . Previously this has been given little attention.

Nuclear Magnetism in Solid ^3He

Magnetic Order in Solid ^3He

^3He atom, practically impenetrable hard sphere, has nuclear spin of $1/2$ and gyromagnetic ratio of $\gamma/2\pi=32.43$ MHz/T. Because of the small mass and the weak interaction potential the atoms are likely to exchange their positions. These atom-atom exchange processes are responsible for the nuclear magnetic ordering of solid ^3He at low temperatures [3,9].

Figure 1.2 shows the ^3He phase diagram in P - T - B representation from Ref. [10]. As mentioned earlier, solid ^3He does not form until the pressure is about 2.93 MPa [11, 12]. The crystal structure for low density solid is body centered cubic (bcc), and hexagonal closed packed (hcp) for high density solid [13]. On cooling the solid at melting density to about 1 mK, the nuclear spins start to order, forming the antiferromagnetic phase (low-field phase or LFP). Because the atom-atom exchange processes are strongly dependent on the interatomic spacing, the increase in solid density dramatically decreases the ordering temperature [14]. For hcp solid ^3He no magnetic ordering is yet observed, although several experiments have pointed to the possibility of a ferromagnetic ground state [15,16,17]. The experimental results from this dissertation is limited to the solid at melting density.

The ordering transition temperature in the LFP decreases with increasing magnetic field [9]. At $B_T=0.392$ T, the triple point of the phase diagram is met, where three phases coexist [18]. Above the critical field $B_{c1}=0.45$ T, a transition to a different ordered phase occurs. This phase, called high-field phase (HFP) has an upper critical field expected to be about 20 T [19] and is surrounded by the paramagnetic disordered phase (PP).

The following is a brief summary of the experimental progress to date in nuclear magnetism in solid ^3He .

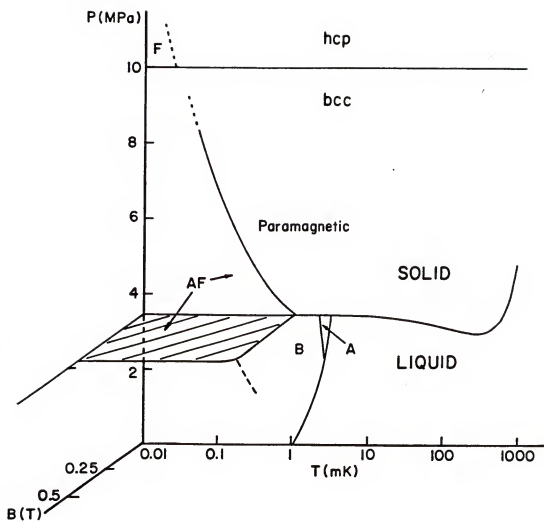


Figure 1.2 The P - T - B phase diagram of liquid and solid ${}^3\text{He}$. A and B are the superfluid ${}^3\text{He}$ A and B phases; AF is the solid ${}^3\text{He}$ antiferromagnetic ordered state; bcc, body-centered cubic; hcp, hexagonal close packed. The solid ordering temperature T_N decreases with the molar volume. Taken from Adams [10].

Thermodynamic Experimental Results

In 1974, Halperin *et al.* [3] first observed magnetic ordering of solid ^3He at $T_N \sim 1$ mK in a Pomeranchuk cell using the latent heat of liquid-solid conversion. Over the temperature range of about 200 μK , the entropy was reduced by about 80% of $R\ln 2$ per mole.

Using the same method, Kummer *et al.* [9] performed the melting pressure measurements in applied magnetic fields up to 1.2 T. Their result for zero field reproduced that of Halperin *et al.* [3]. At the ordering transition T_N , they found the entropy discontinuity of about 0.35 $R\ln 2$. In addition, they showed that T_N decreased slightly with increasing field. However, for fields above $B \sim 0.4$ T, the ordering temperature increased with the field and the character of the ordering also changed. The entropy changed smoothly over the transition. The ordered phase was later known as the HFP. The limiting melting pressure versus B^2 data indicated a high magnetization in the HFP.

More detailed information on the LFP was obtained by Osheroff and Yu [20] from their melting pressure measurements at $B = 14.2$ mT. They found an entropy discontinuity of 0.443 $R\ln 2$ at the ordering transition, confirming the result mentioned above. Below T_N they showed that the melting pressure varied as T^4 , characteristic of an antiferromagnet in which the spin waves have a linear dispersion relation. The spin wave velocity of 8.4 cm/s was obtained. This parameter provided a sensitive test for the theoretical models used to describe the LFP.

Prewitt and Goodkind [21], using a SQUID magnetometer, measured the susceptibility of solid ^3He sample. For fields of 0.4 T or less, the magnetization dropped abruptly on cooling into the ordered phase, which was strong evidence that the LFP is antiferromagnetic. For fields above 0.4 T, the magnetization rose above the Curie law at a temperature they associated with the HFP-PP boundary, previously reported by Kummer

et al. [9]. For fields of 0.42 and 0.46 T, the magnetization showed a sharp decrease at lower temperature, indicating an additional transition now known to be the HFP-LFP transition. Within the HFP, the magnetization leveled off at about half of the saturated magnetization of ^3He M_{sat} , indicating a phase with high magnetization.

Using the same technique, Hata *et al.* [14] measured the magnetization at different molar volumes in the range from 21.02 cm³/mole to 24.14 cm³/mole. They found that the magnetization scaled to the T_N which decreased approximately as $V^{16.5}$, where V is the molar volume.

Solid ^3He magnetization M_s can be obtained from the melting pressure $P(T,B)$ through the Clausius-Clapeyron equation

$$\frac{dP}{dB} = \frac{M_s - M_l}{V_s - V_l}, \quad \text{Eq. (1.2)}$$

where the liquid magnetization M_l is negligible. Osheroff *et al.* [19] measured the limiting melting pressure in the fields as high as 11 T, from which the solid magnetization was obtained. In this work a constant susceptibility of $\chi=1.3 \times 10^{-4}$ per mole at $T=0$ was found for the LFP. At the LFP-HFP transition the magnetization had a discontinuity from 0.19 M_{sat} to 0.6 M_{sat} . Within the HFP, the magnetization monotonically increased to 0.87 M_{sat} at $B=11$ T. Extrapolation to $M=M_{\text{sat}}$ indicated an upper critical field $B_{c2}=21$ T. The direct observation of this critical field therefore requires a magnetic field of about 20 T, which is difficult to reach.

Increase of the solid density hinders the atom-atom exchange processes; the upper critical field B_{c2} therefore decreases to a value accessible in the laboratory at a high density. The work by Fukuyama *et al.* [22] actually mapped out the entire phase diagram in a high density solid ^3He sample (22.69 cm³/mole). The upper critical field B_{c2} was found

to be 5.2 T. This quantity provides an important test on the multiple exchange theory, in which B_{c2} can be calculated exactly [23].

Microscopic Measurements

Two NMR studies of the ordered phases were carried out almost simultaneously in 1980. Adams *et al.* [24] used Pomeranchuk cooling with the drawback that they could only cool their solid ^3He sample slightly below the ordering temperature and their NMR coil contained a polycrystalline mixture of ordered and disordered solid. The advantage was that they were able to raise the magnetic field as high as 3 T, well into the HFP. Osheroff *et al.* [24] used refrigeration by a nuclear demagnetization stage, which allowed much better control of temperature and crystal growth. They were able to study single crystals in the LFP, well below T_N .

Both experiments showed a large shift in the NMR frequency above the Larmor frequency in the LFP. This result excluded immediately the prevailing theoretical view at that time that this phase was simple cubic antiferromagnetic. Such a cubic magnetic configuration would have very little anisotropy in the dipole energy and almost no frequency shift.

Osheroff *et al.* [25] obtained the detailed spectrum of the resonances in the LFP, from which they were able to deduce that a tetragonal symmetry was required and proposed the up-up-down-down (u2d2) nuclear spin structure. This configuration consists of pairs of planes normal to the cubic axis, in which all spins are up, with the next pair of planes having all spins down. However, the NMR data alone can not exclude structures with n planes up and n planes down ($undn$). Benoit *et al.* [26] succeeded in observing magnetic diffraction in a single crystal of ^3He in the LFP. They detected antiferromagnetic ordering with a propagation vector $(1/2, 0, 0)$ consistent with an u2d2 structure, but not

with an $u2d2$ structure. The $u2d2$ structure proposed by Osheroff *et al.* was thus confirmed.

The spectra of Adams *et al* [24] showed a very small frequency shift of 3 kHz, for fields greater than 0.4 T. This frequency shift corresponded to the $0.5 M_{sat}$ magnetization in the HFP. The absence of additional frequency shift indicated a cubic symmetry if the HFP is magnetically ordered. There has been no neutron experiment in the HFP to determine the actual structure. It is most likely to be a canted normal antiferromagnet according to the multiple exchange theory.

In 1982, Osheroff [27] extended NMR measurements to fields up to 0.6 T. Because of the different magnetic structure, each phase had its own characteristic NMR absorption peaks at different frequencies. By adjusting the temperature and the field, Osheroff was able to follow the LFP-HFP boundary, where both LFP and HFP peaks appeared in the same spectra. From the co-existence of the two phases, the LFP-HFP transition was identified as first order. Using the same procedure, the HFP-PP transition was also located. Again both HFP and PP signals were shown in the same spectra. Thus the HFP-PP transition was also first order.

The study of the thermal transport in the LFP is of great interest. Since at milliKelvin temperatures phonons are frozen, magnons are the only heat carriers and magnon-magnon scattering dictates thermal conduction. Feng *et al.* [28] measured the thermal conductivity of ordered solid using the technique based on temperature dependence of the frequency shift in the LFP. The mean free path λ was found to be consistent with magnon umklapp scattering at high temperature portions.

Review of Theory

The Hamiltonian for solid ^3He in a magnetic field can be written in the following form

$$H = H_{ph} + H_{ex} + H_z + H_d, \quad \text{Eq. (1.3)}$$

where H_{ph} , H_{ex} , H_z and H_d are the phonon, exchange, Zeeman and magnetic dipole interactions, respectively. The Zeeman term can be expressed by

$$H_z = -\gamma\hbar\sum_l \vec{I}_l \cdot \vec{B}. \quad \text{Eq. (1.4)}$$

Here γ is the gyromagnetic ratio, I_l the nuclear spin and B the external magnetic field.

The characteristic temperature for phonon interaction is about 10 K, the exchange interaction is about 1 mK, the Zeeman term is 0.778 mK at 1 T and the magnetic dipole interaction is in the order of 100 nK. Therefore nuclear magnetism of solid ^3He at ~ 1 mK is dominated by the exchange interaction and the Zeeman term. The Hamiltonian thus can be written as

$$H = H_{ex} + H_z. \quad \text{Eq. (1.5)}$$

In order to understand the nuclear magnetism of solid ^3He , it is useful to study the high temperature (much higher than the T_N) behavior of the thermodynamic quantities such as entropy, specific heat and the magnetic susceptibility. In such case $\langle H/k_B T \rangle$ is small and a high-temperature expansion can be made, Here k_B is the Boltzmann constant. The description below is model independent.

The partition function for N ^3He atoms is

$$Z = \text{tr}(e^{-\beta H}), \quad \text{Eq. (1.6)}$$

where $\beta = 1/k_B T$. The Helmholtz free energy is

$$F = -\frac{1}{\beta} \ln Z. \quad \text{Eq. (1.7)}$$

upon expanding the exponential factor, the free energy becomes

$$F = -\frac{N}{\beta} \left[\ln 2 + e_2 \frac{\beta^2}{8} - e_3 \frac{\beta^3}{24} + \dots + \frac{1}{2} \left(\frac{\mu_B \beta}{2} \right)^2 (1 + \Theta \beta + \alpha_2 \frac{\beta^2}{8} + \dots) + \dots \right], \quad \text{Eq. (1.8)}$$

where the various parameters such as e_2 , e_3 , Θ and α_2 depend on H_{ex} . Taking the derivative of F with respect to temperature T , the entropy at zero field is

$$S = Nk_B (\ln 2 - e_2 \frac{\beta^2}{8} + e_3 \frac{\beta^3}{12} + \dots). \quad \text{Eq. (1.9)}$$

The specific heat at zero field obtained from the entropy is

$$C_V = \frac{Nk_B}{4} (e_2 \beta^2 - e_3 \beta^3 + \dots). \quad \text{Eq. (1.10)}$$

The susceptibility at zero field is

$$\chi = -\frac{\mu_0 k_B}{V} \left[\frac{\partial^2 F}{\partial B^2} \right] = \frac{C}{T - \Theta + \frac{A}{T}}, \quad \text{Eq. (1.11)}$$

where

$$A = \Theta^2 - \left[\frac{\alpha_2}{8} \right] \quad \text{Eq. (1.12)}$$

and

and

$$C = \frac{\mu_0 R}{V} \left[\frac{\gamma \hbar}{2k_B} \right]^2. \quad \text{Eq. (1.13)}$$

Here μ_0 is the permeability of free space, V the molar volume, and R the gas constant.

Taking the derivative of F with respect to molar volume, the pressure is

$$P = (e_2 \frac{\beta'}{8} - e_3 \frac{\beta'^2}{24} + \dots) + \left(\frac{\gamma \hbar B \beta}{2} \right)^2 \left(\frac{\Theta'}{2} + \frac{\alpha_2 \beta'}{16} + \dots \right), \quad \text{Eq. (1.14)}$$

where the primes indicate differentiation with respect to molar volume V .

The Heisenberg Hamiltonian including only nearest neighbors can be written as

$$H_{ex} = -2J \sum_{i < j} \vec{I}_i \cdot \vec{I}_j, \quad \text{Eq. (1.15)}$$

where I_i and I_j are the nuclear spins for ^3He atoms labeled by i and j , respectively. The summation is over all 8 nearest atoms in the bcc lattice. A positive J would give ferromagnetic ground state, while a negative J results in antiferromagnetic ground state. Before 1975, the Heisenberg nearest neighbor exchange was believed to be able to explain nuclear magnetism in solid ^3He . As the experimental evidences grew [3,9,29,30], this theory became unacceptable. It could not explain the existence of two magnetically ordered phases, the ground state and the nature of the phase transition to the ground state. Theorists were forced to think of modifications to this Hamiltonian.

To illustrate the atom-atom exchange processes, Willard [31] suggested the following picture: suppose you are traveling at rush hour in the metro, the crowd is so dense that people can hardly move; if you want to trade places with your neighbor, it is

practically impossible. But if two or three people agree to move cyclically with you, you can change places. This is exactly the situation for the hard-sphere solid ^3He atoms.

In 1975, soon after the observation of the magnetic ordering by Halperin *et al.* [3] and Kummer *et al.* [9], Hetherington and Willard [32] showed that large ring-exchange terms could account for the first-order transition near 1 mK and gave qualitatively the shape of the magnetic phase diagram.

In their review article in 1983, Roger, Hetherington and Delrieu (RHD) [33] explored in detail Hamiltonians involving two-, three-, and four-particle ring exchange. The calculated results were compared to the experiments, and showed surprising improvements over the Heisenberg nearest neighbor Hamiltonian. Both LFP and HFP were predicted; the magnetic phase diagram calculated for the LFP is u2d2; there was an upper critical field B_{C2} of about 15 T and the shape of the phase boundaries were very similar to the experimental B - T phase diagram. In addition, within the HFP, there was a first-order transition near the triple point of the phase diagram. The second-order transition to the PP extended all the way down to $B=0$. The existence of both first- and second-order transitions has not been verified by experiments. It is generally believed that there is only one HFP-PP transition.

Using only three-adjustable parameter, J_{nn} , J_t and K_p , Stipdonk and Hetherington [34] were able describe reasonable well most of the experimental results on nuclear magnetism in solid ^3He . The exchange Hamiltonian in this model can be expressed by

$$H_{ex} = -J_{nn} \sum_{\langle i,j \rangle} P_{ij} - J_t \sum_{\langle i,j,k \rangle} (P_{ijk} + P_{ijk}^{-1}) - K_p \sum_{\langle i,j,k,l \rangle} (P_{ijkl} + P_{ijkl}^{-1}), \quad \text{Eq.(1.16)}$$

where J_{nn} represents direct two-spin exchange between nearest neighbors, J_t is three-particle exchange frequency, K_p the planar four-particle exchange frequency, illustrated in Figure 1.3. In Eq. (1.16) the two-spin permutation operator P_{ij} is given by

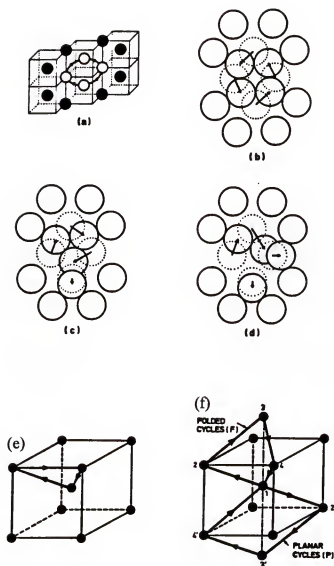


Figure 1.3 Ring exchanges in the bcc lattice. (a) Four atoms and their eight neighbors in a (110) plane; (b), (c), and (d) show four-, three-, and two-particle exchange respectively. (e) Three-particle exchange; (f) two types of four-particle exchange. (e) and (f) are the actual processes believed to be dominant and are not in the (110) plane. Taken from Roger *et al.* [33].

$$P_{ij} = \frac{1}{2}(1 + \sigma_i \cdot \sigma_j), \quad \text{Eq. (1.17)}$$

where the σ_i are the Pauli matrices. The three- and four- spin permutation operators are given by

$$P_{ijk} + P_{ijk}^{-1} = \frac{1}{2}(1 + \sigma_i \cdot \sigma_j + \sigma_j \cdot \sigma_k + \sigma_k \cdot \sigma_i), \quad \text{Eq. (1.18)}$$

and

$$P_{ijkl} + P_{ijkl}^{-1} = \frac{1}{4}(1 + \sum_{\mu < \nu} \sigma_\mu \cdot \sigma_\nu + G_{ijkl}). \quad \text{Eq. (1.19)}$$

where the sum is taken over the six different pairs (μ, ν) among the four particles (i, j, k, l) and

$$G_{ijkl} = (\sigma_i \cdot \sigma_j)(\sigma_k \cdot \sigma_l) + (\sigma_i \cdot \sigma_l)(\sigma_j \cdot \sigma_k) - (\sigma_i \cdot \sigma_k)(\sigma_j \cdot \sigma_l). \quad \text{Eq. (1.20)}$$

Figure 1.4 shows the magnetic phase diagram generated by this exchange Hamiltonian; Figure 1.5 shows the solid magnetization M/M_{sat} versus temperature T .

Recently, Ceperley and Jacucci [35] used Monte Carlo path integral techniques to estimate the importance of a number of exchange processes, and found that two-, three-, four-, five-, and six-particle ring exchanges were all similar in magnitude.

Using the mean-field theory (MFT), $T=0$ properties of the LFP and the HFP were calculated including up to six-particle exchange processes by Godfrin and Osheroff [36]. These properties agreed well with the experimental values using the exchange frequencies calculated by Ceperley and Jacucci [35].

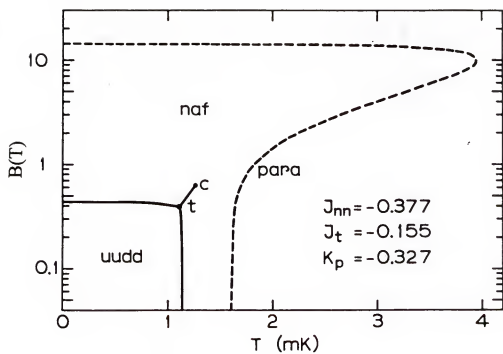


Figure 1.4 Magnetic phase diagram of solid ^3He , generated by three fitting parameters J_{nn} , J_t , K_p in mean-field theory, from H. L. Stipdonk and J. H. Hetherington [34].

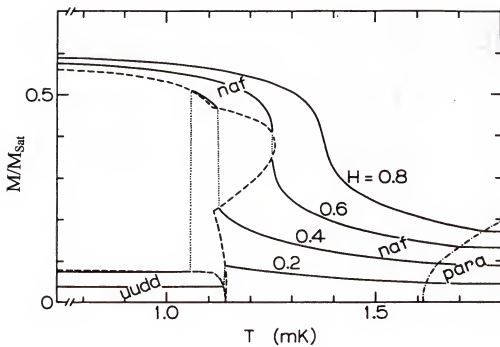


Figure 1.5 Calculated magnetization of solid ^3He M/M_{Sat} versus temperature T , using the same set of fitting parameters, from H. L. Stipdonk and J. H. Hetherington [34].

CHAPTER II EXPERIMENTAL TECHNIQUES

Introduction

In this chapter, the design and the performance of the dilution refrigerator and the nuclear demagnetization stage will be briefly presented. Various thermometers used in the melting pressure thermometry work and the solid ^3He experiment are described in detail, from the principles on which they are based to the design and construction.

Before going to the presentation of the cryostat, a few words about the thermometry are given here. Thermometers in general can be divided into two main categories: primary thermometers and secondary thermometers. A primary thermometer determines the temperature from first principle and is based on a well understood physics. It is often used as a calibration standard and rather sophisticated in measuring equipment. The ^{60}Co nuclear orientation (NO) thermometer used in this work is a primary thermometer [37,38,39,40]. A secondary thermometer must be calibrated at least at one known temperature. It is widely used in low temperature physics for its simplicity, quickness as well as precision in measuring the temperature. The magnetic susceptibility of platinum (Pt NMR) used in this work is a secondary thermometer.

Cryostat

The cryostat used in this work consists of the dilution unit, the PrNi_5 nuclear demagnetization stage, the gas pumping system and the floating table.

The dilution unit (still-to-mixing chamber), model DRP-43, was purchased from S.H.E. Corp., 4174 Sorrento Valley Blvd., San Diego, CA. 92121 (now Biomagnetic

Inc.), installed as a joint effort of Drs. Adams and Ihas. It has a maximum helium circulation rate of 1 mmole/sec, but is usually operated at 0.5 mmole/sec or lower, providing a minimum temperature of 5 mK.

Since the graduation of Y. H. Tang in 1987, the dilution refrigerator had a leak problem after cooldown to milliKelvin temperatures for 3 or 4 days. The problem was the design of the indium o-ring seal in the mixing chamber which did not provide sufficient pressure for a vacuum seal. It was modified, and the leak problem was solved. The pumping and return lines were cleaned, whereupon a large amount of Edwards 9B3 diffusion pump oil was found in a home made filter sitting in the top of the cryostat, in the gas circulation line and in the mixing chamber. The dilution refrigerator has not given any problem since this repair and cleaning.

The PrNi_5 nuclear demagnetization stage was reconstructed. The amount of PrNi_5 was increased from 0.6 mole (12 rods, each about 7 mm in diameter and 6 cm long, purchased from Ames Laboratory, Iowa State University, Ames, IA. 50011) to 1.0 mole (20 rods). They were cadmium soldered to 392 copper wires of 0.8 mm diameter. The copper wires are bundled together with the top end welded to a copper flange thermally connected to the mixing chamber through a tin heat switch, and the bottom end welded to a small copper flange. Figure 2.1 shows the cryostat below the mixing chamber.

Figure 2.2 shows the cooling power of the dilution refrigerator at the circulation rate $\dot{n}=0.75$ mmole/sec. The cooling power \dot{Q} can be fitted approximately to the form

$$\dot{Q} = aT_m^2 - b \quad \text{Eq. (2.1)}$$

where T_m is the mixing chamber temperature. A recent paper on the cooling power of the dilution refrigerator can be found in Ref. [41]. For this dilution refrigerator, the measured values at $\dot{n}=0.75$ mmole/sec are $a=16.4$ mW/K² and $b=6.5$ μ W.

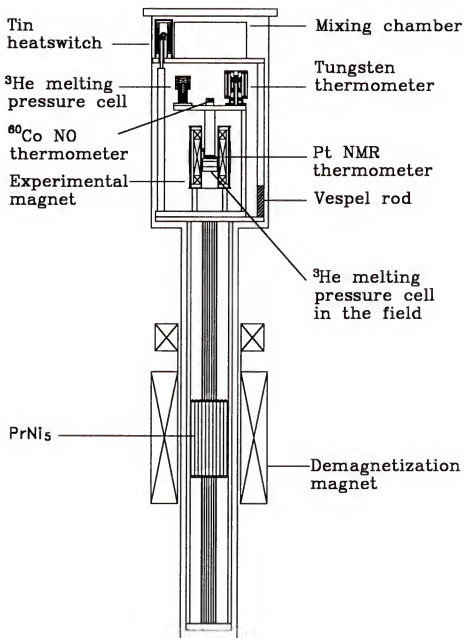


Figure 2.1 Experimental arrangement for the ^3He melting pressure thermometry experiment and the solid ^3He experiment. Not drawn to scale.

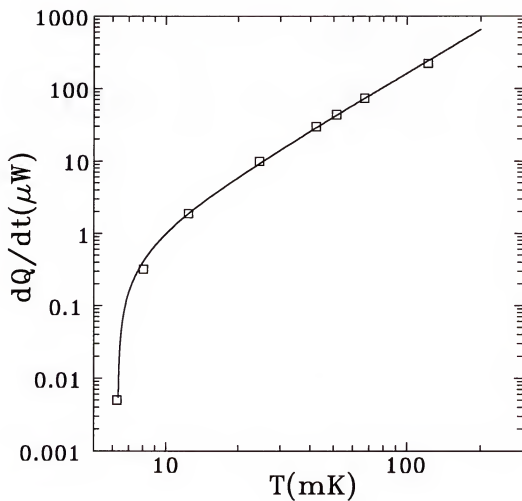


Figure 2.2 Cooling power of the dilution refrigerator. The solid line is the fit to the experimental data (squares). See text for detail.

The choice of PrNi₅ (a hyperfine enhanced nuclear paramagnet) versus copper as nuclear refrigerant depends on the temperature requirement of the experiment. A Copper nuclear demagnetization stage can reach temperatures below 100 μ K. The minimum temperature for a PrNi₅ nuclear demagnetization stage, on the other hand is around 0.3 mK because of the nuclear magnetic ordering of the PrNi₅. The advantage of a PrNi₅ demagnetization stage is that it can remove more entropy for the same amount of material, therefore providing more cooling power.

Because of the hyperfine enhancement of the external field by a factor of 12.2 [42], the entropy curves for PrNi₅ are shifted to higher temperature where the dilution refrigerator has higher cooling power for precooling the PrNi₅. At 25 mK and at 6 T, the dilution refrigerator can take 78% of the entropy out of PrNi₅. While for copper, even at 8 mK and at 8 T, only 8% reduction of the entropy is achieved.

The entropy of the non-interacted nuclear spins of PrNi₅ can be expressed by

$$\frac{S}{R} = \frac{x}{2} \left\{ \coth\left(\frac{x}{2}\right) - (2I+1) \coth\left[\frac{x(2I+1)}{2}\right] \right\} + \ln\left(\frac{\sinh[x(2I+1)/2]}{\sinh(x/2)}\right). \quad \text{Eq. (2.2)}$$

In the above expression, $x = \alpha \mu_B g B / k_B T$, $\alpha = 12.2$ is the enhancement factor, μ_B the Bohr magneton, g the electronic Lande factor, B the magnetic field, T the temperature and $I = 5/2$ the nuclear spin. Eq. (2.2) is only a function of B/T , therefore for an ideal adiabatic demagnetization the ratio B/T remains the same. If B_i and T_i are the initial field and temperature, and B_f and T_f are the final field and temperature, then

$$T_f = \frac{B_f}{B_i} T_i. \quad \text{Eq. (2.3)}$$

Since the demagnetization field is linearly proportional to the current in the demagnetizing magnet, Eq. (2.3) can be written as

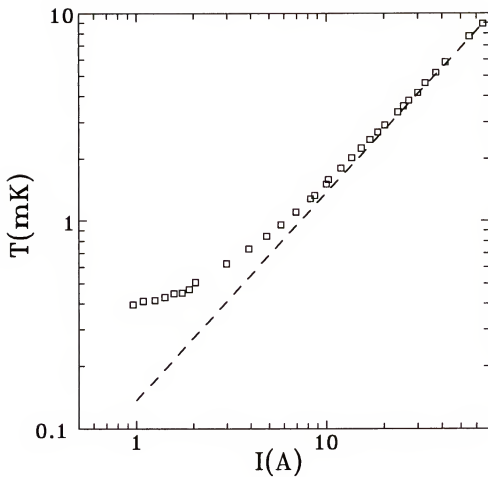


Figure 2.3 A typical demagnetization of the PrNi_5 nuclear stage measured by a Pt NMR thermometer. The central field of demagnetization magnet to current ratio B/I is 0.11 T/A.

$$T_f = \frac{I_f}{I_i} T_i, \quad \text{Eq. (2.4)}$$

where I_i and I_f are the initial and final current. The above equations can not be used in the limit $B_f \rightarrow 0$, because the assumption of non-interactions of the nuclear spins. For very small B_f Eq. (2.3) is replaced by

$$T_f = \frac{T_i}{B_i} \sqrt{B_f^2 + b^2}, \quad \text{Eq. (2.5)}$$

where b is the internal field resulting from the interaction of the nuclear spins. Figure 2.3 shows a typical demagnetization of the nuclear stage measured by a Pt NMR thermometer. The slight deviation from the ideal adiabatic behavior (the dashed line) above 1 mK is probably due to the eddy current in the PrNi₅ nuclear stage and considerable amount of ³He (~0.07 mole) needed to be cooled in the demagnetization process. The severe deviation below 1 mK is because of the nuclear magnetic ordering of PrNi₅.

There are two separate experiments presented in this thesis. In the first experiment, ³He melting pressure versus temperature P - T was measured precisely from 0.5 mK to 25 mK. Melting pressures were from the ³He melting pressure cell located outside the field (see Figure 2.1). Temperatures were determined from a ⁶⁰Co NO primary thermometer and Pt NMR, calibrated against the NO thermometer, as a secondary thermometer. The tungsten superconducting transition fixed point was used for comparison of the tungsten superconducting transition temperature measured in this work with that determined by NIST. All the above thermometers will be described in the following sections.

In the second experiment, melting pressures of ³He in various magnetic field (from the cell inside the magnet, see Figure 2.1) were studied extensively between 0.5 mK to 2

mK. Temperatures were determined from the same ^3He melting pressure thermometer, located outside the field. The tungsten and ^{60}Co NO thermometers were not present in the experimental arrangement.

^3He Melting Pressure Thermometer

^3He Melting Pressure Cell Design

The ^3He melting pressure cell consists of two parts (see Figure 2.4): 1. The ^3He chamber, where the mixture of solid and liquid ^3He is located. Silver powder of 700-Å-diameter serves as a heat exchanger for thermal contact between liquid ^3He and the cell body made of 99.99% purity silver. 2. The flexible metal diaphragm, which drives the bottom plate of the capacitor up or down according to the pressure of the ^3He , provides the measurement of capacitance as a function of pressure.

Straty and Adams [43] and the most recent review paper by Adams [44] give a very detailed description on the construction of the melting-pressure cell. Briefly, the displacement of the diaphragm with pressure is given by

$$y = \frac{3a^4 P}{16Et^3}, \quad \text{Eq. (2.6)}$$

where y is the displacement, a is the radius of the diaphragm, t is its thickness, P is the pressure and E is the Young's modulus of the material, usually BeCu or coin silver. In this experiment coin silver was used. It is clear from Eq. 2.6 that a thinner diaphragm would give greater deflection, therefore more sensitivity for a given pressure change. A larger diaphragm would also give the same effect. However, the limitation is that the stress s in the material, given by

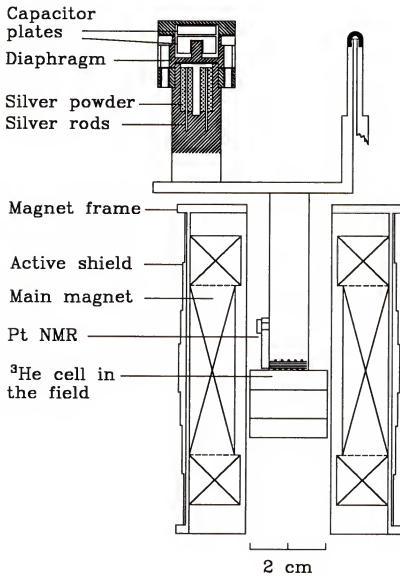


Figure 2.4 Melting pressure cell, Pt NMR thermometer and superconducting magnet used in the experiment.

$$s = \frac{3a^2 P}{4t^2} \quad \text{Eq. (2.7)}$$

must be kept well below the yield stress. The radius of the diaphragm should also be small (less than 2 cm is desirable) because of space limitations. This is important because a large ^3He space not only uses a lot of ^3He , but also creates a longer thermal time constant at low temperatures.

The two melting pressure cells used in this work have the same size. The diaphragms, made of coin silver, are 1.17 cm in diameter and 0.76 mm thick. If a cell is not designed properly, the capacitor will be hysteretic. Hysteresis checks of the diaphragms were performed at liquid nitrogen temperature over the working pressure range of 2.76 MPa to 3.52 MPa. After cycling the pressure several times, hysteresis could be reduced to within 200 Pa.

The ^3He chamber was partially filled with 2.45 gram silver powder packed under 200 atm pressure, giving 4.90 m² surface area. The ratio of open volume to total volume is 0.27. It is important that there be sufficient open volume for the solid ^3He to grow, otherwise solid formed inside the pores of the powder may cause long thermal time constant, and the melting pressure will be elevated above that of the bulk solid if the liquid-solid interface is in the pores [45]. Eight 0.76 mm diameter silver rods, embedded in the powder, were diffusion welded to the silver body to increase the thermal contact between the powder and the silver body.

^3He Melting Pressure Cell Calibration and Measurement

Figure 2.5 shows the electronic diagram for measuring the capacitance of the melting pressure thermometer. The lock-in amplifier (PAR 5204) has an internal oscillator, which supplies a sine wave to the capacitance bridge through an isolation transformer

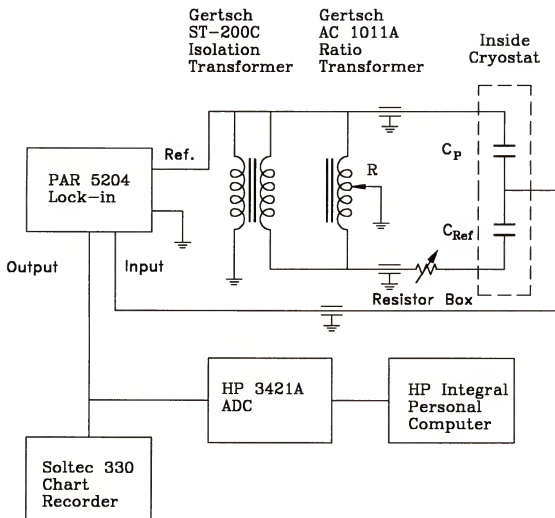


Figure 2.5 Electronic diagram for measuring the capacitance of ^3He melting pressure cell.

(Gertsch ST-200C). The ratio transformer (Gertsch AC 1011A) can be used to measure the cell capacitance C_p . For the ideal bridge, the ratio of output and input voltage is

$$\frac{V_O}{V_I} = \frac{(x-1)C_p + xC_{ref}}{C_p + C_{ref}}, \quad \text{Eq. (2.8)}$$

where x is the ratio transformer setting and C_{ref} is the fixed reference capacitance. The capacitor was thermally anchored to the mixing chamber of the dilution refrigerator. At the balance, $V_O=0$; therefore

$$\frac{C_p}{C_{ref}} = \frac{x}{1-x}. \quad \text{Eq. (2.9)}$$

Thus the capacitance of the melting pressure cell can be obtained from the ratio transformer setting x . As will be discussed later, the absolute value of C_p is not used. In fact all that is needed in the experiment is the calibration of pressure as a function of the ratio transformer setting $P(x)$.

A more realistic analysis of the circuit considering cable capacitance and resistance shows that the denominator of Eq. (2.8) is replaced by $C_p + C_{ref} + C_l$ where C_l is the capacitance of the coaxial cable which connects to the lock-in amplifier. In a real measurement, C_l can be several times of C_{ref} or C_p . Therefore, the output signal V_O is reduced considerably. If the highest possible resolution is needed, a preamplifier placed on top of the cryostat can be used.

The lock-in amplifier used to measure the cell pressure in the magnetic field was Ithaco 391A.

Figure 2.6 shows the ^3He gas handling panel for loading the pressure cells. ^3He gas which contains less than 8 ppm of ^4He was drawn into the dipstick inserted in the liquid ^4He dewar. The liquid-nitrogen cooled charcoal trap is used to trap any air that might

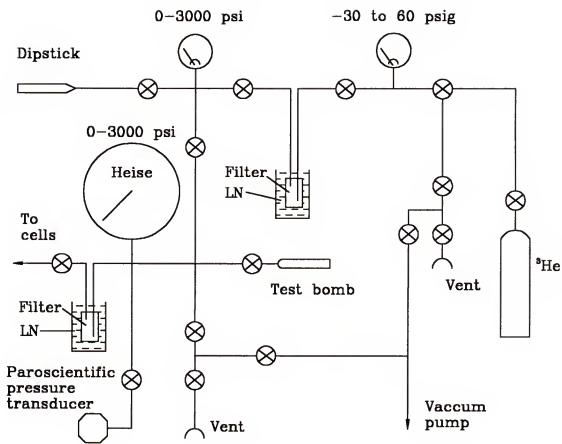


Figure 2.6 ^3He gas handling panel

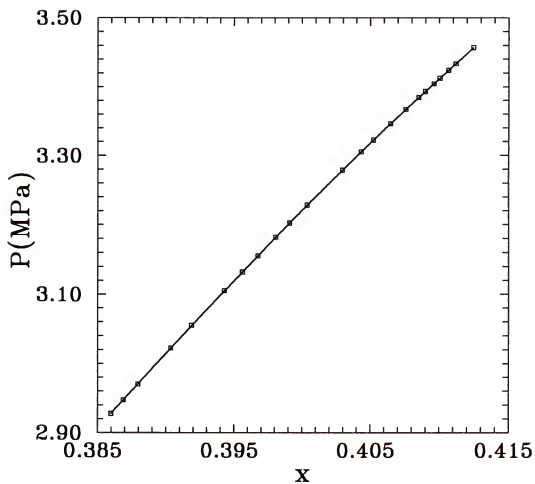


Figure 2.7 Melting pressure cell calibration P - x with the Paroscientific pressure gauge.

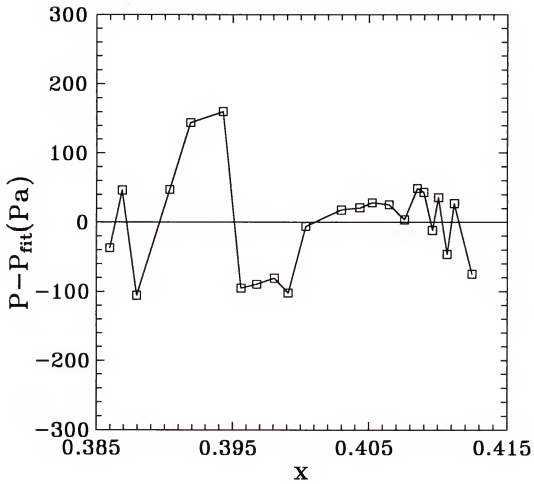


Figure 2.8 Pressure difference between the measured points and those from the polynomial fit of Eq. (2.10).

remain in the lines or in the ^3He gas. The pressure of ^3He gas can be increased by raising the dipstick to the warm part of the dewar. The pressure transmitted to the cells is monitored both by the Heise pressure gauge and the Paroscientific pressure gauge (Model 9200 AT, Paroscientific, Inc., Redmond, WA). The latter has an accuracy of 0.5% and is used for obtaining the pressure calibration $P(x)$.

When the cryostat was cooled to about 0.8 K, the pressure calibration was performed. The melting pressure cells were loaded with ^3He and the diaphragms were trained by slowly cycling the pressures between 3.52 MPa and 2.82 MPa. When up and down pressures for the same ratio setting were different by less than 300 Pa, pressure versus capacitance calibration data were recorded. Figure 2.7 shows the calibration of $P(x)$. The data points are fitted to the following polynomial form:

$$P = a_0 + a_1x + a_2x^2 + a_3x^3, \quad \text{Eq. (2.10)}$$

with a maximum deviation from the fit of less than 200 Pa (see Figure 2.8). There is about 1.4 kPa hydraulic pressure head between the pressure transducer and the cell and it is included in the first term a_0 in Eq. (2.10). For this work, absolute pressure is not required. In fact, the melting pressure is measured relative to the fixed points along the melting curve, to be discussed in detail in Chapter III.

Thermal contact with the solid is through the liquid; hence, shorter time constants are obtained if the solid fraction is small. An initial pressure of 3.4 MPa was used in the experiments, which gave a few percent of the solid near 1 mK temperatures [12]. In obtaining the pressure minimum for use as a fixed point, an initial pressure filling of 3.0 MPa was used. This procedure was necessary in the cells which had only 27% open space used in the experiment to avoid elevation of the melting pressure. The pressure minimum with the cell filled at 3.4 MPa pressure was found to be 1.6 kPa higher than the pressure minimum for filling at 3.0 MPa.

Pt NMR Thermometer

Pt NMR Thermometer Design

The pulsed platinum NMR thermometer was made by Dr. Kirk Uhlig. It consisted of two parts: 1. The platinum brush, made of 200 platinum wires of 25 μm diameter and of 5N purity. One end of the brush was inserted into the slit of the platinum block holder. The bundle and the block were then welded together in an argon gas environment. Then, acrylic spray coating (Krylon No. 1303A) was used to insulate the wires. The brush was cut to 1 cm length. 2. The rf pick-up coil for measuring the magnetization of the platinum. This pick-up coil, with an inductance of 6.4 μH , made of a 50 μm diameter copper wire, had two layers each with 60 turns. The total length of the coil was 5 mm and the diameter was 2 mm. The pick-up coil was placed over the Pt brush and was fixed to its position by a tiny amount of GE varnish.

Principle of Pt NMR Thermometer

The physics on which the Pt NMR thermometer is established is the Curie's law:

$$M = \frac{CB}{T}, \quad \text{Eq. (2.11)}$$

where M is the static magnetization of the platinum, B is the external static magnetic field provided by the superconducting magnet, T is the temperature and C is the Curie constant.

Initially the nuclear magnetization M lies along the direction of the static field B , see Figure 2.9. Then a small sinusoidal field $B_y = B_1 \sin \omega t$ is applied for the duration of several full cycles. This pulse tips M away from its previous direction along the z axis by a small angle θ . M will precess with the Larmor frequency $\omega_n = \gamma B / 2\pi$ around the z axis while it recovers to equilibrium determined by the spin-spin relaxation time τ_2 . γ is the

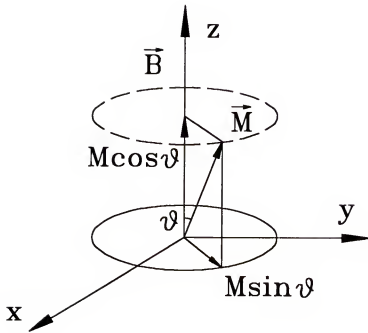


Figure 2.9 Principle of Pt NMR thermometry

gyromagnetic ratio of the platinum. The component $M \sin \theta$ which rotates in the x - y plane induces a voltage

$$u = b \omega_n M \sin \theta \quad \text{Eq. (2.12)}$$

in the pick up coil wound around the Pt brush. Here b is a constant related to the inductance of the coil and the filling factor of the platinum; M is proportional to $1/T$. The signal is thus inversely proportional to the temperature as expressed by

$$\frac{u(T_1)}{u(T_2)} = \frac{M(T_1)}{M(T_2)} = \frac{T_2}{T_1}, \quad \text{Eq. (2.13)}$$

where T_1 and T_2 are two different temperatures of the platinum. If T_1 is known, then T_2 can be calculated from the ratio of the two signals.

It is important to note that the temperature measured is the temperature of the nuclei. The coupling between the nuclei and the electrons follows the Korringa relation

$$\tau_1 T_e = K \quad \text{Eq. (2.14)}$$

where T_e is the conducting electron temperature, τ_1 is the spin-lattice relaxation time and K is the Korringa constant. For platinum, K is about 30 sec mK, therefore τ_1 is very short even at 1 mK, giving rapid equilibrium between the nuclear spins and the lattice. In principle, by measuring the spin-lattice relaxation τ_1 , temperature can be determined through Eq. (2.14). However, this method should be employed with great caution. In some experiments, deviations from the Korringa relation have been observed for platinum and these deviations are contributed to the magnetic impurity in the platinum [46].

Because of the difficulty in measuring the platinum magnetization in absolute value, temperature can not be determined through Eq. (2.11). Therefore, the Pt NMR

thermometer is a secondary thermometer which requires calibration at a known temperature. In this work, the calibration was against a ^{60}Co NO primary thermometer (to be discussed in next section). The results of the calibration will be discussed in detail in Chapter III.

Electronics for Pt NMR

Figure 2.10 shows the schematic diagram for measuring the Pt susceptibility used in Tang's thesis work [47]. The Matec power supply for the low-noise amplifier and the cascode amplifier did not regulate the dc voltage when the voltage in the utility line changed. It was replaced by a power supply made by Acdc Electronics Inc. The HP3325A synthesizer provides a continuous sinusoidal pulse to the electronic gate controlled by a burst pulse timer. The frequency of the pulse is set to the Larmor frequency of platinum given by

$$\nu = \frac{\omega}{2\pi} = \frac{\gamma}{2\pi} B = 8.786B \frac{\text{MHz}}{\text{T}}. \quad \text{Eq. (2.15)}$$

The peak-to-peak voltage V_{pp} ranges from 200 mV to 500 mV, depending on the temperature region where the Pt NMR thermometer is used, such that it does not cause heating in the measurements. The duration of the pulse is governed by the gate, $t = nT$, where n is the gate number and T is the period of the sinusoidal pulse. The tipping angle θ of the magnetization can be adjusted by the attenuator, V_{pp} or the gate number. Below 2 mK, θ is set to a few degree. Figure 2.11 shows a plot of circuit response versus frequency. The peak location is the resonant frequency of the tank circuit. The free induction decay signal from the Pt NMR thermometer is amplified by a low noise amplifier and a cascode amplifier, then fed to the Nicolet 204A digital oscilloscope. The digitized

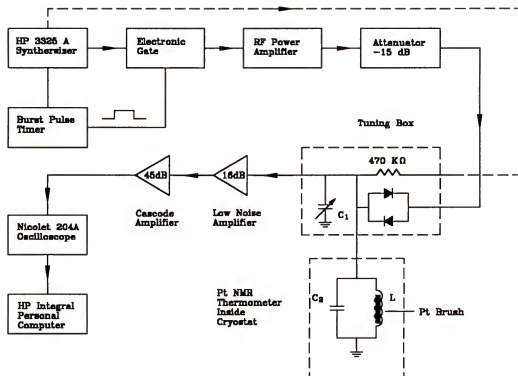


Figure 2.10 Electronics for measuring the Pt NMR temperature.

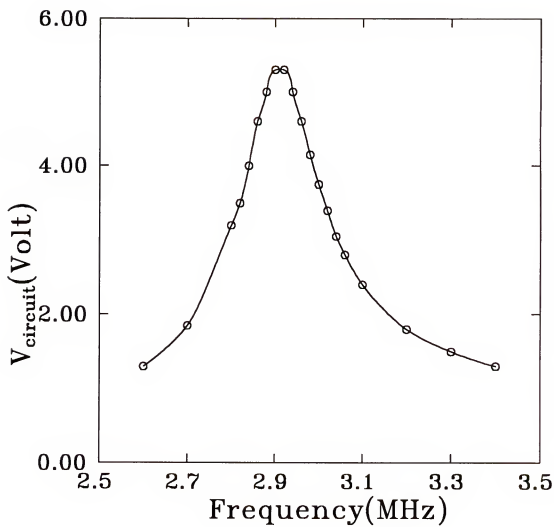


Figure 2.11 Tuning of the Pt NMR circuit. The circuit frequency is adjusted to the Larmor frequency ν determined by Eq. (2.15) to get the maximum amplification of the Pt FID signal.

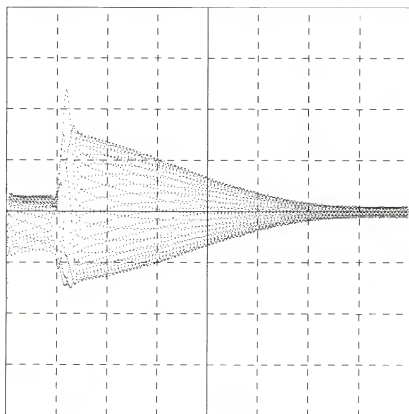


Figure 2.12 Digitized Pt FID signal at $\nu=3.625$ MHz, taken at $T=4.5$ mK. Horizontal axis 26 $\mu\text{sec}/\text{div}$. and vertical axis 0.25 V/div.

FID signal (see Figure 2.12) was then integrated by the computer to give the temperature reading.

⁶⁰Co Nuclear Orientation Thermometer

Nuclear orientation thermometry offers one of the most direct and accurate means of measuring the temperature below 1 K [37,38,39,40]. In this work, a ⁶⁰Co in an hcp ⁵⁹Co single crystal γ -ray anisotropy thermometer was used in conjunction with a Pt NMR thermometry of ³He. The NO thermometer is a primary thermometer, since the theory is well established and understood. Essentially, it measures the degree of ordering of the nuclear spin system in thermodynamic equilibrium. The temperature is thermodynamic since it is derived from the Boltzmann factor. In this section, the physics on which the NO thermometer is based, is described, together with some remarks on the sample preparation and its use in the experiment. The discussion of the results will be deferred to Chapter III.

The theory of NO thermometry is well described in Refs [37,40]. The normalized directional distribution of γ radiation emitted from an oriented ⁶⁰Co nuclear spin system is given by

$$W(\theta, T) = 1 - Q_2 U_2 F_2 B_2 P_2(\cos \theta) - Q_4 U_4 F_4 B_4 P_4(\cos \theta), \quad \text{Eq. (2.16)}$$

where T is the nuclear spin temperature, θ is the angle between the direction of emission of the γ ray and the orientation axis (c -axis of the single crystal). U_2 , U_4 and F_2 , F_4 are the angular momentum deorientation coefficients and angular distribution coefficients respectively, which can be calculated from the decay scheme of the radioactive nuclei. For ⁶⁰Co, $U_2=0.9393744$, $U_4=0.7977240$ and $F_2=-0.4477023$, $F_4=-0.3043790$ [37]. Q_2 and Q_4 are solid angle correction factors, which are calculated for the particular situation in this work (see appendix). $P_2(\cos \theta)$ and $P_4(\cos \theta)$ are Legendre polynomials. The

temperature dependence comes from B_2 and B_4 , which are related to the nuclear spin distribution moments $f_k(I)$ by

$$B_k(I) = \frac{2k!}{(k!)^2} I^k \left[\frac{(2I+1)(2k+1)(2I-k)!}{(2I+k+1)!} \right]^{1/2} f_k(I), \quad \text{Eq. (2.17)}$$

where

$$f_2(I) = \frac{1}{I^2} \left[\sum_{m=-I}^I m^2 p(m) - \frac{I(I+1)}{3} \right], \quad \text{Eq. (2.18)}$$

and

$$f_4(I) = \frac{1}{I^4} \left[\sum_{m=-I}^I m^4 p(m) - \frac{(6I^2 + 6I - 5) \sum_{m=-I}^I m^2 p(m)}{7} + \frac{3I(I-1)(I+1)(I+2)}{35} \right].$$

Eq. (2.19)

Here $p(m)$ is thermal equilibrium of the nuclear spin population

$$p(m) = \frac{\exp(m\Delta_{hf} / k_B T)}{\sum_{m=-I}^I \exp(m\Delta_{hf} / k_B T)}. \quad (2.20)$$

For ^{60}Co , the nuclear spin $I=5$ and the hyperfine splitting, $\Delta_{hf} = 6.0725$ mK [39,40], has been measured with high accuracy by NMR on oriented nuclei (NMR-ON) [40]. Figure 2.13 shows the γ -ray directional distribution at various temperatures. In the experiment, the γ -ray detector is usually placed at $\theta=0$ to obtained the maximum variation of the

anisotropy $W(0,T)$. At high temperature $T=\infty$, the radiation is isotropic. As the temperature lowers, the nuclear spins become more ordered (see Eq.(2.20)) and the radiation anisotropy appears. At $T=0$, there is no radiation at $\theta=0$. Figure 2.14 shows the temperature dependence of the anisotropy $W(0,T)$ at $\theta=0$ and its sensitivity (right hand vertical axis). The maximum temperature sensitivity for the ^{60}Co NO thermometer is at $T=6$ mK and its useful range is 1.5 mK-50 mK.

Table 2.1 lists $W(0,T)$ versus temperature for ^{60}Co NO thermometer, generated by Eq. (2.16) and without the solid angle corrections.

Table 2.1 ^{60}Co NO anisotropy $W(0,T)$ versus temperature T

$T(\text{mK})$	$W(0,T)$	$T(\text{mK})$	$W(0,T)$
1.0	0.00232	9.5	0.61152
1.5	0.01762	10.0	0.63320
2.0	0.04892	11.0	0.67213
2.5	0.09092	12.0	0.70590
3.0	0.13816	13.0	0.73528
3.5	0.18699	14.0	0.76090
4.0	0.23525	15.0	0.78331
4.5	0.28173	16.0	0.80297
5.0	0.32583	17.0	0.82028
5.5	0.36729	18.0	0.83557
6.0	0.40607	19.0	0.84911
6.5	0.44222	20.0	0.86115
7.0	0.47585	22.0	0.88148
7.5	0.50711	24.0	0.89784
8.0	0.53616	26.0	0.91115
8.5	0.56314	28.0	0.92211
9.0	0.58821	30.0	0.93122

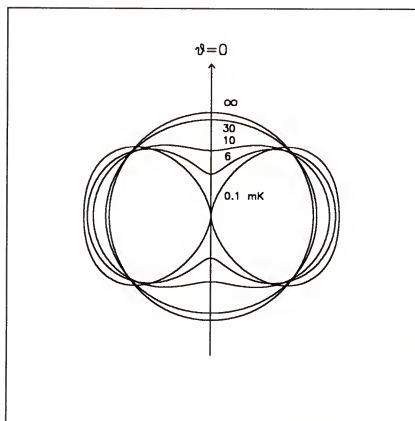


Figure 2.13 γ -ray directional distribution of ^{60}Co at various temperatures (in mK) generated by Eq. (2.16).

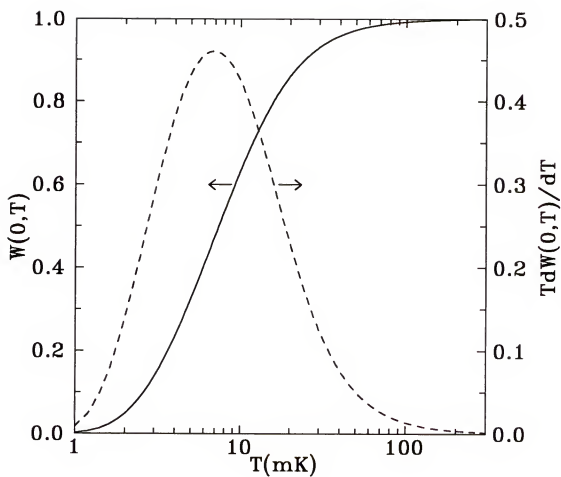


Figure 2.14 γ -ray anisotropy $W(0,T)$ of ^{60}Co NO thermometer and its sensitivity $TdW(0,T)/dT$.

Measuring Anisotropy and the Determination of Temperature

Experimentally, the anisotropy $W(0, T)$ is determined by

$$W(0, T) = \frac{C_c - B_c}{C_w - B_w}, \quad \text{Eq. (2.21)}$$

where C_w is the warm γ -ray count at a sufficient high temperature, where $W(0, T) \approx 1$, C_c is the cold count at temperature T and the B 's are the corresponding background. $W(0, T)$ is then used to determine the temperature T through Eq. (2.16).

Figure 2.15 shows the diagram of electronics used in the γ -ray measurement. The distance from the NO thermometer to the liquid nitrogen cooled germanium detector was 30 cm. The detector has a 40-mm diameter and 35-mm long germanium crystal, Model 7229P, made by Canberra Industry, Inc., Meriden, CT. The signal from the detector was then amplified (EG&G ORTEC 672) and converted to digital form (Nuclear Data 579 ADC). A computer-based multichannel analyzer was used and the output of the γ -ray spectrum was displayed on the computer screen and could be saved in a file. Figure 2.14 shows the NO thermometer γ -ray spectrum at 2.5 mK and at 210 mK from the actual γ -ray measurement in the melting pressure thermometry experiment. The procedure in measuring the NO temperature will be described in detail in Chapter III.

Sample Preparation and Thermal Contact

The NO thermometer obtained from the Oxford Instruments, Inc. Concord, MA, uses ^{60}Co in a hexagonal ^{59}Co monocrystal which provided the polarizing magnetic field. ^{60}Co was produced by the neutron capture of ^{59}Co . The cobalt sample, which was soldered with indium to a OFHC copper block, was 1.3 mm x 1.3 mm x 8 mm long, with the c-axis along the long dimension.

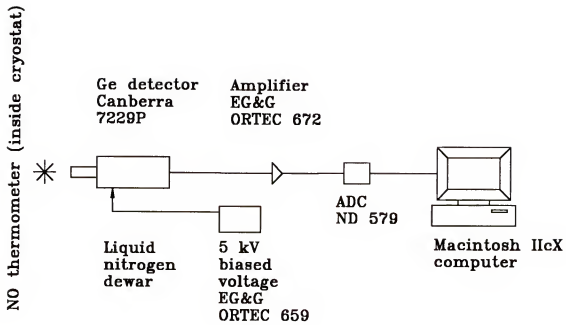


Figure 2.15 Electronics for measuring the γ -ray from the ^{60}Co NO thermometer.

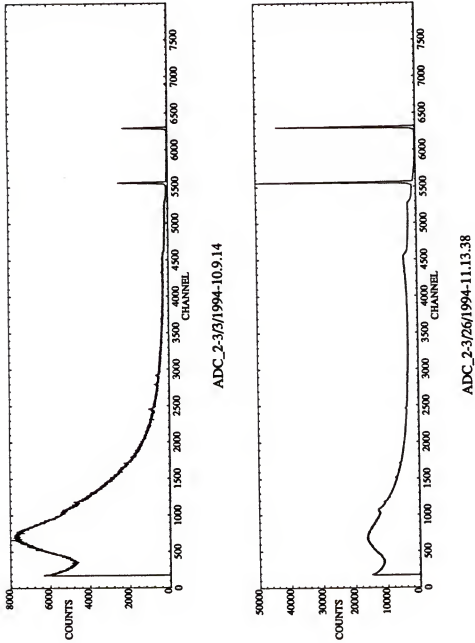


Figure 2.16 γ -ray spectrum of ^{60}Co NO thermometer at 2.5 mK (ADC_2-3/3/1994-10.9.14) and at 210 mK (ADC_2-3/26/1994-11.13.38).

As mentioned earlier, the temperature obtained through Eq. (2.16) is that of the ^{60}Co nuclei. The temperature of the ^3He was needed for the thermometry. The time for achieving the thermal equilibrium is characterized by the spin-lattice relaxation time τ_1 . At high temperatures, i.e., $T \gg \Delta_{hf}$ τ_1 obeys the Korringa relation Eq. (2.14). The Korringa relation is no longer valid at low temperature and τ_1 tends to level off to a constant value. The $T=0$ limiting τ_1 is given by

$$\tau_1 = \frac{2K}{\Delta_{hf}}. \quad \text{Eq. (2.22)}$$

which is about 20 sec given by Ref. [40]. The γ -ray counting interval is usually in the order of several minutes or hours, the thermal response is thus not a problem.

The temperature difference between the Pt NMR thermometer and the NO thermometer was significant in the experiment and could not be ignored. In fact, the NO thermometer could not be cooled to below 2.5 mK. This was because the absorption of β particles in the ^{60}Co source produced a self-heating of 650 pW/ μCi [37], which for this particular NO thermometer of $\sim 5 \mu\text{Ci}$ would be 3 nW. As a result of the finite thermal resistance between the NO thermometer and the Pt NMR thermometer, the NO thermometer read higher temperature than that of the Pt NMR thermometer. In the ^3He melting pressure thermometry work to be described in next chapter, this presents no problem since the two temperatures are closely related.

Tungsten Superconducting Fixed Point Thermometer

Design of the Tungsten Superconducting Fixed Point Thermometer

Tungsten superconducting transition temperature has been determined by NIST to be 15.53 mK in the device designated SRM 768 using a germanium resistance

thermometer which was calibrated against a noise thermometer and a ^{60}Co NO thermometer in a previous run. The tungsten superconducting fixed point thermometer (tungsten thermometer for short) is intended as a reference standard for use in calibrating other thermometers.

Figure 2.17 shows the tungsten thermometer. The black spot at the center is the tungsten sample provided by NBS [47]. It is 0.13 cm in diameter, 0.64 cm long, has a RRR value of 1000 and a purity of 99.999%. It was spark cut from an ingot of tungsten. The surface damage caused by the cutting was removed by gentle abrasion with 600 grit silicon carbide sandpaper followed by final polishing with 20 and 2 μm diameter aluminum oxide powder. The tungsten sample is silver painted and inserted into the slot on top of the vertical silver post thermally anchored to the nuclear stage. The cryoperm was provided by Dr. F. Pobell and the niobium shield was home made.

A mutual inductance coil was used to detect the superconducting transition. The primary coil which was connected to the reference signal output of the lock-in amplifier (see Figure 2.18), and the secondary coil, which picks up the induced voltage signal, was connected to the input of the lock-in amplifier. On warming of the tungsten sample from the superconducting state to the normal state, the expulsion of flux causing a voltage jump in the secondary coil, which can be monitored by the chart recorder.

In using the tungsten thermometer two things require particular attention: heating by the primary coil and the effect of a dc magnetic field on the tungsten superconducting transition temperature.

Heating Problem

The introduction of current into the primary coil generates heat in two ways: I^2R loss in the primary coil, eddy current heating in the tungsten sample and in the silver post. Since the coil is heat sunk to the nuclear stage, Joule heating will not heat the tungsten

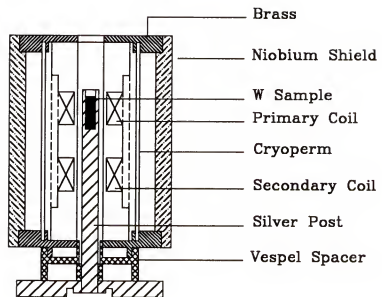


Figure 2.17 Tungsten superconducting fixed point device.

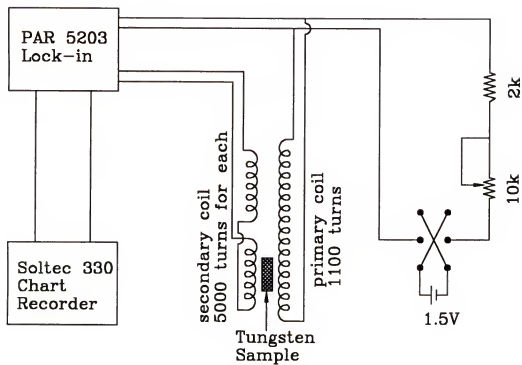


Figure 2.18 Electronic diagram for measuring the W thermometer.

sample directly. The eddy current heating in the tungsten sample and the silver post can be calculated from

$$\dot{Q} = \frac{V}{32\rho} \dot{B}^2 d^2, \quad \text{Eq. (2.23)}$$

where V is the tungsten sample or silver volume exposed to the time varying magnetic field B . For tungsten, the resistivity $\rho=5 \times 10^{-9} \Omega\text{cm}$ and the diameter $d=0.13 \text{ cm}$. For silver, $\rho=1.5 \times 10^{-9} \Omega\text{cm}$, the silver volume exposed to the magnetic field is about 1/3 of the tungsten volume. For a sinusoidal current in the primary coil, after averaging over one full cycle, Eq. (2.23) becomes

$$\dot{Q} = \frac{VB_{pp}^2 \pi^2}{64\rho} v^2 d^2. \quad \text{Eq. (2.24)}$$

The lock-in amplifier supplied a ac current $I_{pp}=140 \mu\text{A}$, with $v=400 \text{ Hz}$. The magnetization jump ΔM at the tungsten superconducting transition had about $0.1 \mu\text{V}$ signal, which was easy to be seen in a chart recorder with $0.25 \mu\text{V}$ sensitivity setting in the lock-in. The magnetic field $B_{pp}=2.2 \mu\text{T}$ was obtained through

$$B = \alpha I, \quad (2.25)$$

where $\alpha=0.0158 \text{ T/A}$ is the coil constant. The calculated Joule heating was 0.98 nW . The eddy current heating is 36 pW for tungsten and 40 pW for the silver. The Joule heating was sunk to the mixing chamber, therefore it did not cause the temperature gradient between the tungsten sample and the Pt NMR or the melting pressure thermometer. The eddy current heating is too small to cause any appreciable temperature gradient.

The Effects of DC Magnetic Field

The critical field for tungsten is 0.012 T and a few μT field will have a profound effects on the tungsten thermometer. The first effect of a small ambient DC magnetic field on the tungsten thermometer is the suppression the superconducting temperature T , which is given approximately by [48]

$$B_c(T) = B_c(0) \left[1 - \left(\frac{T}{T_c} \right)^2 \right]. \quad (2.26)$$

A more accurate equation, differing only by a few percent from Eq. (2.26), is given by the BCS theory [49]. Therefore the transition temperature in the field needs to be solved from the Eq. (2.26). If B is much smaller than the critical field B_c , near T_c the temperature suppression may be calculated from

$$\Delta T = T_c(B) - T_c = B \left(\frac{dB_c}{dT} \right)^{-1} \Big|_{T=T_c}. \quad (2.27)$$

The second effect of the magnetic field is that it causes the tungsten to supercool. Because of the supercooling, the transition temperature on cooling becomes lower than that on warming. The maximum supercooling can be calculated from the equation derived from the Ginzburg-Landau theory [50]:

$$\Delta T_s = T_s - T_c = \frac{B}{2.4\kappa} \left(\frac{dB_c}{dT} \right)^{-1} \Big|_{T=T_c}. \quad (2.28)$$

where $\kappa=0.09$ [47] is the G-L parameter for the tungsten sample.

For the above reasons, a small ambient field needs to be avoided. The shielding of the tungsten thermometer will be discussed in next chapter.

CHAPTER III
³HE MELTING PRESSURE THERMOMETRY EXPERIMENT

Tungsten Superconducting Transition

After the ³He pressure cells were loaded at a pressure of 3.39 MPa, the dilution refrigerator was cooled down to less than 10 mK temperature in a few hours. The melting pressure at tungsten superconducting transition T_W was measured with the Pt NMR magnet and the demagnetization magnet off. This is because a small stray magnetic field from either magnet will significantly affect the tungsten superconducting transition temperature. Figure 3.1 shows the traces of the tungsten magnetization versus the melting pressure cell temperature simulated from the chart recorder.

As shown in the Figure 3.1 there was a considerable supercooling observed, as the system was cooled or warmed through T_W , indicating about a few μ T magnetic field trapped on the W sample, although the magnetic field shielding was carefully done. The warming melting pressure value was $P_W - P_N = 56,437$ Pa, while the cooling melting pressure was $P_c - P_N = 54,067$ Pa. Here P_N is the melting pressure at the solid ordering transition to be discussed later. These corresponded to T_W of 15.3 mK and 14.7 mK according to the melting pressure scale measured in this experiment (to be discussed later).

The sources of trapped field of about a few μ T in the tungsten sample were unknown. The tungsten sample was shielded by the Cryoperm, which had been degaussed at room temperature to eliminate any possible field left by machining. Outside the Cryoperm, there was a superconducting niobium shield. Before the cryostat cooldown the liquid helium dewar was surrounded by μ -metal. This procedure should reduce the

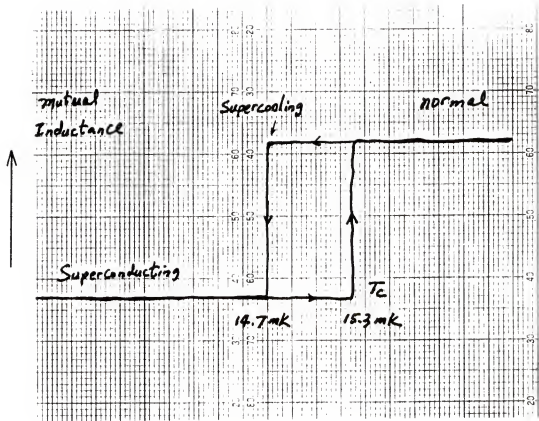


Figure 3.1 The measured tungsten superconducting transition temperatures, simulated from the chart recorder. Recorded is the mutual inductance versus cell temperature converted from the melting pressure. The warming and cooling rates are $100 \mu\text{K/h}$.

ambient field to a few tenth of a μT . Putting a few μT in the vertical direction through the primary coil in an attempt to cancel the trapped field did not solve the supercooling problem. The trapped field apparently had horizontal components. The tungsten superconducting transition for zero field estimated following Eqs. (2.27) and (2.28) was 15.4 mK. This is 0.13 mK (0.8%) smaller than the NIST value [47] for the T_W .

Temperature and Melting Pressure Measurements

After measurement of the tungsten superconducting transition temperature, the Pt NMR magnet was raised to 0.390 T, where the Pt NMR signal was optimal. Using the Kepco power supply Model ATE6-100M, the PrNi_5 nuclear stage was also magnetized to about 4.8 T, corresponding to a 45 A current in the demagnetization magnet. The power supply was controlled by a home-made 0-5 V voltage ramping circuit, which could divide the above voltage range into $2^{16} - 1$ steps. Both magnets were persisted. After precooling by the dilution refrigerator to an initial temperature of 9.0 mK in about 36 hours, the demagnetization of the nuclear stage was performed. The demagnetization rate was 45 A-20 A in 4 hours, 20 A-10 A in 3 hours and 10 A-2.5 A in 3 hours.

In the process, the melting pressure cells were cooled through the ^3He superfluid A transition, the AB transition, and the solid ordering transition at zero field and at 0.39 T. The demagnetization was then stopped at 2.5 A and the nuclear stage was left undisturbed overnight for all the components to be cooled properly.

The next morning the germanium γ -ray detector was moved to the position whose orientation had been accurately determined by the laser beam before the cryostat was closed up. The position of the germanium detector could be further tuned to $\theta=0$ by counting the γ -ray in several positions, each for 2 hours while maintaining the demagnetization stage at 0.7 mK. The germanium detector position was chosen to be where the γ -ray counts were the lowest. The detector was within less than $\Delta\theta=0.5^\circ$ to the

axial direction $\theta=0$. The error of $\Delta T/T$ caused by misalignment $\Delta\theta=0.5^\circ$ was calculated from Eq. (2.16). At 2.5 mK, the lowest temperature which the NO could reach, $\Delta T/T=0.08\%$, rather insignificant compared to errors from the counting statistics of the γ -ray. At higher temperatures $\Delta T/T$ is even smaller 0.08%. The germanium detector should not be near the cryostat when the demagnetization stage field was high, because of possible damage to the the detector. Because of a few nW heat leak into the nuclear stage, the ^3He cells and other components warmed up at a rate of 2-8 μK per hour. To stabilize the temperature, extremely slow demagnetization of the nuclear stage was needed.

In taking the γ - ray counts of the NO thermometer, the heat leak was offset by a very slow demagnetization of the nuclear stage, typically 10 mA to 20 mA per hour. The temperatures were thus held constant for 8 hours to within 5 μK by monitoring the melting pressures of the ^3He cells, shown in Figure 3.2. After each hour of counting, the γ -ray spectrum was saved on the computer for later analysis. There was about 3 second dead time in saving it on a file and displaying on the computer screen. The cells were warmed to a higher temperature to repeat the above process. The NO warm counts were measured much later at 210 mK (where the anisotropy ~ 1) for 20 hours in order to minimize statistical error.

When the temperature of the nuclear stage reached about 7 mK, the heat switch between the mixing chamber and the nuclear stage was closed and demagnetization was not necessary. The temperatures were rather easily regulated by connecting the output of the melting pressure cell to the LR-130 temperature controller, which supplied a feedback current to the heater located on the top flange of the nuclear stage.

The γ -ray counts and the background for the selected windows of 1.17 MeV and 1.33 MeV were calculated. Each window was 19 keV or 90 channels. The whole spectrum had 8192 channels. The γ -ray counts and the background were used in Eq. (2.23) to obtain the anisotropy $W(0,T)$. Because of the high resolution of the germanium detector, the two γ -ray peaks were well separated and each peak gave an independent-

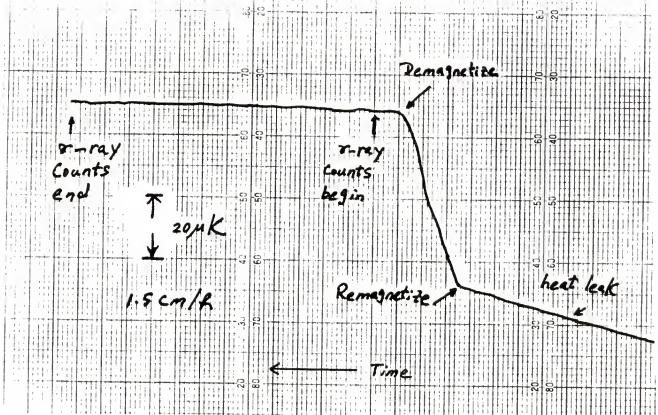


Figure 3.2 Temperature control in taking the ^{60}Co γ -ray counts, simulated from the chart recorder. Recorded is the melting pressure versus time, with chart recorder speed 1.5 cm/h.

temperature determination. The average temperature from the two peaks were used for the NO thermometer because of very small M3/E2 mixing ratio [39], which gave the two peaks the same anisotropy. Using the long counting time, a precision of 0.2% in $W(0,T)$ was obtained, which translated to 0.6% in temperature at 4 mK and 0.9% at 20 mK. Because of the same anisotropy of the two peaks, more accessible NaI γ -ray detector could have been used. In a NaI detector γ -ray spectrum, the above two peaks would be partially overlapped.

To make the Pt NMR temperature measurement, the tank circuit resonant frequency was adjusted to the Larmor frequency of 3.265 MHz by changing the tuning capacitor C_1 . The time integral of the Pt NMR FID signal digitized by the Nicolet 204A was calculated by a computer and the result together with the melting pressure cells output was stored in a data file and printed out for later analysis.

The melting pressures from both cells were recorded continuously on the chart recorder. The driving voltages from both lock-in amplifiers were $2.5 V_{pp}$. Their frequencies were 625 Hz and 844 Hz, chosen to be different so that they did not interfere with each other and were away from the harmonics of the 60 Hz utility-line frequency.

Figure 3.3 shows the signatures of various fixed points on the melting curve. The solid ordering transition is a first order transition; therefore, in going through the transition the melting pressure remains constant until the latent heat (about $0.4T_N/R\ln 2$ per mole, to be discussed in detail in the next chapter) is supplied. The melting pressure slope changes by about a factor of 3. This transition is unique in that it does not show a noticeable supercooling.

The superfluid AB transition is also a first order transition, but the latent heat is much smaller (about $1.3 \times 10^{-4} T_B/R\ln 2$ per mole). Therefore the melting pressure slope change is barely noticeable. Supercooling occurs to about $0.7 T_{AB}$ in the initial cooling from the A phase to the B phase. On a second cool back from above T_{AB} , very little supercooling (only to about $0.97 T_{AB}$) was observed, indicating that somehow the B phase

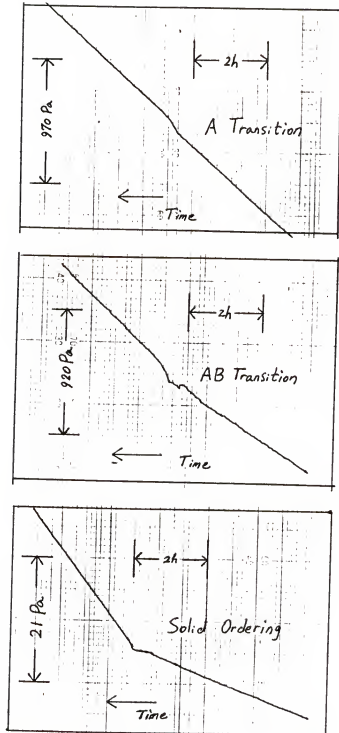


Figure 3.1 Signatures of various fixed points on the melting curve. The superfluid A transition $T_A=2.505 \text{ mK}$; the AB transition $T_{AB}=1.948 \text{ mK}$ and the solid ordering transition $T_S=0.934 \text{ mK}$.

had memory in the first cool through [51]. The warm up transition $B \rightarrow A$ always occurs at the same temperature and it is used as a fixed point. In a magnetic field, the B transition temperature decreases with field. At 0.39 T, no B transition was observed on the cooldown. The nucleation of the B phase is a very interesting topic [51,52,53]. When the superfluid ^3He is confined by microscopically smooth surfaces, supercooling to as low as $0.19T_{AB}$ has been observed [52].

The superfluid A transition is second order. So there is no latent heat, but the specific heat of the liquid ^3He decreases by a factor of 2.6 from the A phase to the normal phase. In the chart recorder, there is an obvious kink. This is because the temperature of the cell is drifting and the load (the specific heat of liquid ^3He) suddenly decreases at the A transition. The kink is observable only when the system is not in thermal equilibrium. Therefore when the warming or cooling rate is reduced, it becomes difficult to detect. In a magnetic field, the A transition will split into transitions with an A_1 phase and an A phase [54].

Table 3.1 lists the melting pressure differences between the fixed points obtained in this work together with those by other authors. The pressure minimum was measured just before the warm up of the cryostat with the cell filled at a pressure of about 3.0 MPa. This procedure is necessary in a cell with a small fraction of open volume in order to avoid elevation of the melting pressure when the liquid-solid interface is in the packed powder.

The ^3He sample used in this experiment had ^4He impurity of less than 8 ppm, determined by a mass spectrometer leak detector. Small ^4He contamination makes almost no effect on the results in the Table 3.1 because of the ^3He - ^4He phase separation. Below 50 mK, maximum possible ^4He concentration in solid ^3He is about 1 ppm, and even smaller in liquid ^3He . The effect of ^4He on the melting pressure at high temperatures is rather different and can be estimated [55]. At 0.4 K, the maximum decrease in melting pressure by 10 ppm ^4He impurity is 30 Pa, which is less than the experimental uncertainty in Table 3.1.

Table 3.1. Pressure differences between fixed points

	$P_N - P_A$ (Pa)	$P_N - P_{AB}$ (Pa)	$P_A - P_{min}$ (Pa)
Halperin <i>et al.</i> [3]	5,230 ± 20	3,240 ± 16	502,600 ± 100
Avenel <i>et al.</i> [56]	5,210	3,210	
Greywall [4]	5,252 ± 10	3,252 ± 5	502,050 ± 100
Fukuyama <i>et al.</i> [7]	5,272 ± 26	3,250 ± 19	
Hoffmann <i>et al.</i> [57]	5,210 ± 50	3,150 ± 30	502,640 ± 80
this work	5,234 ± 30	3,243 ± 20	502,574 ± 100

Results and Discussions

The absorption of β particles in the ^{60}Co source produced a self-heating \dot{Q} which causes the temperature T_γ of the Co source to be higher than that of the melting pressure cell or the Pt NMR thermometer at temperature T . The relationship between these two temperatures, \dot{Q} , and the prefactor of thermal conductance $K=kT$ is

$$\dot{Q} = \frac{k}{2}(T_\gamma^2 - T^2). \quad \text{Eq. (3.1)}$$

Neither \dot{Q} nor k are quantities that may be easily determined. However, this presents no difficulty when the NO thermometer is used with the Pt NMR secondary thermometer for which the susceptibility χ is given by the Curie law,

$$\chi = \frac{C}{T}, \quad \text{Eq. (3.2)}$$

where C is the Curie constant. Combining Eqs. (3.1) and (3.2), we have

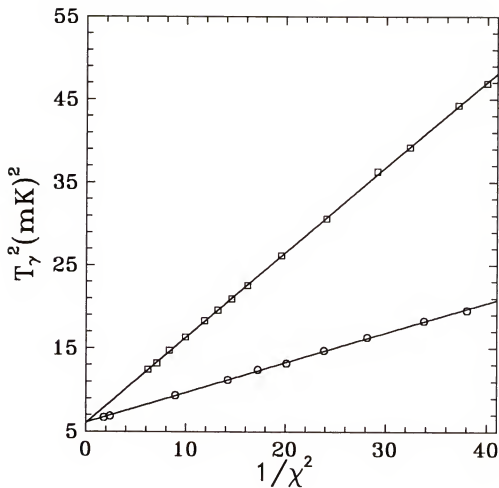


Figure 3.4 T_γ^2 of the ^{60}Co NO thermometer versus $1/\chi^2$ of the Pt NMR thermometer for two different tipping pulses. The intercept and slopes determine the constants $2\dot{Q}/k$ and C , respectively, in Eq. (3.3).

$$T_Y^2 = \left(\frac{C}{\chi}\right)^2 + \frac{2\dot{Q}}{k}, \quad \text{Eq. (3.3)}$$

As indicated by Eq. (3.3), a plot of T_Y^2 vs $1/\chi^2$ is a straight line with intercept $2\dot{Q}/k$ and slope C^2 . Thus the two constants, C and $2\dot{Q}/k$, required for obtaining T may be determined with high accuracy. The measurements of T_Y^2 vs $1/C^2$ for two different pulse tipping angles are shown in Figure 3.4. These are in the temperature range 0.78 to 3.56 mK for the smaller pulse and 2.5 to 6.9 mK for the larger pulse. The two values for the intercept $2\dot{Q}/k$ are 6.120 and 6.062 (mK)², in excellent agreement. The Curie constant C for the Pt NMR thermometer is determined by the entire straight line rather than a single temperature and has a uncertainty of 0.5%.

The measurements of the melting pressure and temperature between T_N and 25 mK used in the polynomial fit of $P_m(T)$ include 63 points. The temperatures used in the fit were those from the Pt NMR thermometer, calibrated against the NO thermometer, for the low temperature region. Above 7 mK, temperatures were determined exclusively from the NO thermometer by using Eq. (3.3).

When the value for P_{mn} is adjusted to match that of Fogle *et al.* [8], the two sets of points $P(T)$ in the region of overlap from 15 to 25 mK are indistinguishable. Thus, in order to provide a single scale extending up to 250 mK, their data above 15 mK were combined with the ones from this work to provide a fit between T_N and 250 mK.

Using the similar fitting forms as Halperin *et al.*[3] and Greywall [4,6],

$$P(T) - P_N = \sum_{n=-4}^5 A_n T^n, \quad \text{Eq. (3.4)}$$

the coefficients obtained in the fit are as follows:

$$\begin{aligned}
A_{-4} &= 0.78405848 & A_{-3} &= -4.5968629 & A_{-2} &= 9.5436359 \\
A_{-1} &= -10.041752 & A_0 &= 8.5580332 & A_1 &= -4.4431076 \\
A_2 &= 1.5962639 \times 10^{-2} & A_3 &= -3.8815407 \times 10^{-5} & A_4 &= 7.1230765 \times 10^{-8} \\
A_5 &= -6.0945626 \times 10^{-11}.
\end{aligned}$$

Temperatures are in mK and pressures are in kPa, given relative to P_N rather than to P_A (used by Halperin *et al.* [3] and Greywall [4,6]), since T_N can be identified more readily and with greater precision than T_A . Alternatively, the reference pressure may be taken as P_A or P_{min} by making use of the differences in pressure between the various points given in Table 3.1. For $T < T_N$, the melting pressure can be represented with a single term in T :

$$P(T) - P_N = B_0 - B_1 T^4, \quad \text{Eq. (3.5)}$$

with $B_0 = 0.1987$ kPa and $B_1 = 0.2611$ kPa/(mK)⁴ measured in the solid ³He experiment [58] to be described in next chapter.

Comparison of the fixed points from this work to that of others is made in Table 3.2.

Table 3.2. Comparison of fixed point among different groups

	T_A (mK)	T_{AB} (mK)	T_N (mK)	$T_C(0)$ (mK)	Method
Halperin <i>et al.</i> [3]	2.752±0.11	2.179	1.100		Latent heat
Avenel <i>et al.</i> [56]	2.75±0.05	2.20±0.03	1.08±0.1		Pt NMR
Kummer <i>et al.</i> [9]	2.68±0.21	2.10	1.03		Latent heat
Paulson <i>et al.</i> [59]	2.625	2.054		1.055	LCMN
Alvesalo <i>et al.</i> [60]	2.79±0.14	2.16±0.02		1.04	Pt NMR
Greywall [6]	2.491±0.02	1.932±0.015	0.931±0.008	0.931	LCMN, C _v
Fukuyama <i>et al.</i> [7]	2.477±0.026	1.933±0.021	0.914±0.012		Pt NMR
This work	2.505±0.025	1.948±0.020	0.934±0.009		⁶⁰ Co, Pt NMR

where T_A , T_{AB} , and T_N are the superfluid ^3He A, A-B, and solid ordering transitions, respectively. $T_C(0)$ is the A transition at zero pressure. In some references, T_N is denoted by T_S .

The Halperin temperature scale [3] is thermodynamic and based on the assumption that the melting pressure slope is given by the Clausius-Clapeyron equation, from which

$$\frac{T}{T_A} = \exp \left[\int_0^{P-P_A} (\Delta Q / \Delta V)^{-1} dP \right], \quad \text{Eq. (3.6)}$$

where the integration variable P is the pressure difference from the A transition, ΔQ and ΔV are the molar latent heat and molar volume change on melting, respectively. $\Delta Q / \Delta V$ was measured in a Pomeranchuk cell as a function of melting pressure. This scale gave $T_A = 2.752 \pm 0.11 \text{ mK}$.

Avenel *et al.* [56] used the Korringa relation for the platinum

$$T_1 T = K, \quad \text{Eq. (3.7)}$$

where T_1 is the spin-lattice relaxation time. By measuring T_1 and using the Korringa constant $K = 30.2 \text{ msec K}$, determined from an osmotic pressure thermometer (a primary thermometer) between 30 and 300 mK, they found $T_A = 2.75 \pm 0.05 \text{ mK}$.

Kummer *et al.* [9] used the same latent heat technique as the Halperin *et al.* [3] in their temperature measurements in the solid ^3He experiment, when the two ordered magnetic phases were first observed. They identified $T_A = 2.68 \text{ mK}$

Paulson *et al.* [59] used a LCMN susceptibility thermometer, which was calibrated against a germanium resistance thermometer in the temperature range of 0.3 to 1.1 K. In particular, they assumed $\Delta = 0.1 \text{ mK}$ in the following Curie-Weiss law

$$T = \frac{C}{\chi} + \Delta, \quad \text{Eq. (3.7)}$$

where χ is the magnetic susceptibility of the LCMN and C the Curie constant. This scale yielded $T_A=2.625$ mK. The previous provisional La Jolla scale [61] based on the unpublished primary noise thermometry gave $T_A=2.6 \pm 0.1$ mK.

The Alvesalo *et al.* [60] used the same technique as Avenel *et al.* [56], but adopted a slightly different Korringa constant $K=29.9$ msecK for platinum, determined from a calibration against a ^{60}Co NO thermometer between 7 to 35 mK from Ahonen *et al.* [62]. This scale gave $T_A=2.79 \pm 0.14$ mK.

The Greywall temperature scale of 1986 [6] is the most complicated among all the scales known. It was based on the susceptibility of LCMN, which was calibrated against the tungsten superconducting transition $T_W=15.57 \pm 0.05$ mK, assigned by the NBS. In order to determine the other parameter in Eq. (3.7), the specific heat of normal liquid ^3He measured by LCMN was assumed to be linear in temperature. This scale gave $T_A=2.49 \pm 0.02$ mK, considerable lower than previous T_A determinations.

Fukuyama *et al.* [7] calibrated their Pt NMR thermometer against the Greywall 1985 melting pressure scale in the temperature range between 15 to 45 mK. Assuming the Curie law for their Pt NMR susceptibility, this scale gave $T_A=2.477 \pm 0.026$ mK.

While $T_A=2.505 \pm 0.025$ mK found in this work agreed within 1% to the results of Greywall and Tokyo scales, the method and physical law on which the scale was based is straightforward. The ^{60}Co NO thermometer used is a primary thermometer, where the theory is well understood. The Pt NMR thermometer used was calibrated in the entire temperature range shown in Figure 3.4 rather than at a single point. The calibration and extrapolation was very reliable, unlike other cases where the extrapolation spanned a tremendous range.

The P - T relationship measured by NIST [8] were of high precision. Their temperatures were determined by a Josephson junction noise thermometer (a primary thermometer), several superconducting fixed points, and a CMN thermometer for interpolation. Their results were in good agreement with Greywall above 15 mK. However, below 15 mK, their temperatures read systematically higher temperatures than those of Greywall. At 7 mK, the lowest temperature in their measurements, the deviation from Greywall's scale was 1.5% after adjusting the T_C assignments for the superconducting samples in Greywall's SRM 768 device (provided by NBS). The T_C assignments used by Greywall were from NBS 1983 scale, which were slightly different from the NIST values. The original Greywall melting pressure scale actually agreed to within $< 1\%$ of the NIST scale. This again shows the complexity of Greywall's temperature scale, susceptible to the T_C assignments of the superconductive devices used in his measurements.

The NIST melting pressure scale did not reach sufficiently low temperatures to include the ^3He superfluid A transition. However, the A transition temperature T_A could be obtained by extrapolating their P - T data above 7 mK, using the Clausius-Clapeyron equation. Using the molar volume data by Grilly [11], and the specific heat data on solid and liquid ^3He of Greywall [7,63], Bremer [55] was able to calculate the A transition temperature T_A from the melting pressure through the following equation

$$\frac{d^2P}{dT^2} = \frac{C_s(T) - C_l(T)}{(V_s - V_l)T}, \quad \text{Eq. (3.8)}$$

where $C_s(T)$ and $C_l(T)$ were the specific heat for the solid and the liquid, respectively. In their calculation, $T_A=2.68$ mK was obtained by using Greywall's $P_A-P_{mn}=502,050$ Pa (see Table 3.1). This value is probably in error by about 600 Pa. Using the larger P_A-P_{mn} values

of other authors, the calculated T_A 's are considerably lower. Table 3.3 lists the T_A values calculated from this procedure.

Table 3.3. Calculated T_A from the melting pressure difference

	$P_A - P_{min}$ (Pa)	T_A (mK)
Halperin <i>et al.</i> [3]	$502,600 \pm 100$	2.54
Greywall [4,6]	$502,050 \pm 100$	2.68
Hoffmann <i>et al.</i> [57]	$502,640 \pm 80$	2.52
this work	$502,574 \pm 100$	2.55

Comparison of this temperature scale, given by the fit, Eq. (3.4) to that of Greywall, Fukuyama *et al.*, and NIST in the temperature range 0.9 to 20 mK is shown in the Figure 3.5. In order to make this comparison, the differences in pressures measured by different workers, given in Table 3.1, were adjusted by normalizing all pressure differences between T_A and T_N to correspond to this work. Then, the various temperatures were calculated from the fits $P(T)$ given by different workers. In addition the fixed points of different workers are shown separately when they do not agree with the calculated temperature. As already mentioned, the temperatures of Fogle *et al.* [8] agree quite well with this work in the region of overlap. Then, since their P - T relationship was based on a primary (noise) thermometer, they were used to extend P - T relationship of this work to 250 mK. The deviation between the Greywall scale and this work is $\sim 1\%$ in the few mK range, thus the experimental results currently based on Greywall's scale should not require adjustment to the scale measured in this work.

Figure 3.6 shows the melting pressure slope dP/dT versus temperature. The dP/dT minimum from this work is lower than that of Greywall. The unphysical behavior above 15 mK from Fukuyama *et al.* is probably because of the improper polynomial fit.

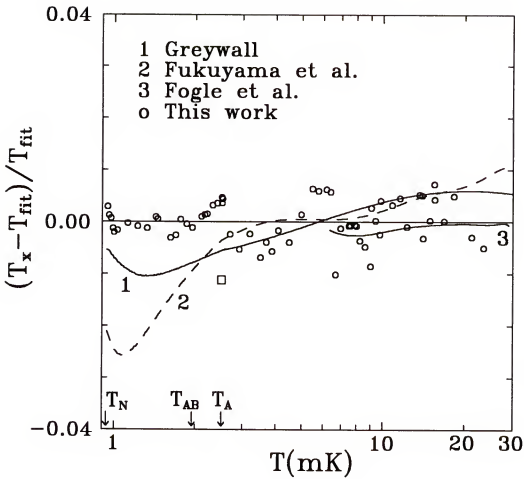


Figure 3.5 Comparison of different temperature scales. Temperatures were converted from the melting pressure $P(T)$ given by each author. Open circles are from this work. \square is T_A from Fukuyama *et al.*

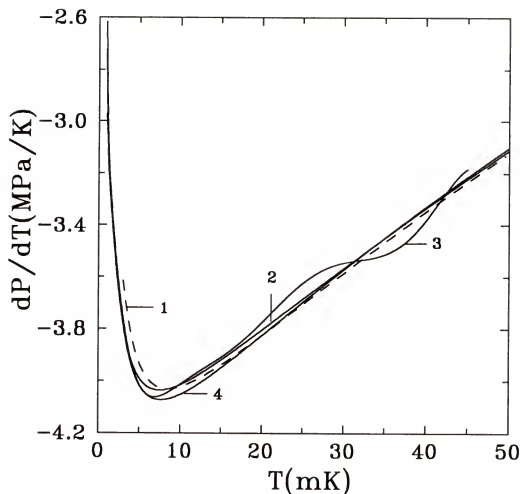


Figure 3.6 Melting pressure slope dP/dT versus temperature. 1. Halperin *et al.* [3]; 2. Greywall [6]; 3. Fukuyama *et al.* [7] and 4. this work. The slope minimum near 7.5 mK from this work is lower than that of Greywall [6]. The unphysical behavior above 15 mK from Fukuyama *et al.* is probably due to the improper polynomial fit.

In conclusion, the ^3He melting pressure versus temperature, using a primary thermometer and a calibrated secondary thermometer, from 0.5 mK to 25 mK has been measured. Combining our results with those of Fogle *et al.* [8], at higher temperatures, a functional form $P(T)$ and values for the fixed points for the melting pressure temperature scale up to 250 mK were provided. The temperature scale described here is in good agreement with the NIST values above 7 mK, if their melting pressure minimum is adjusted to the one measured in this work. The deviation from Greywall's temperature scale and that of Fukuyama *et al.* is around 1%, which is in the combined experimental error. The temperatures determined by Halperin *et al.* read systematically higher temperature of about 10% above T_A . The T_A values determined by Avenel *et al.*, Kummer *et al.*, Paulson *et al.* and Alvesalo *et al.* listed in Table 3.2 are 10%, 7.2%, 6% and 12% higher than the T_A value determined here. Using the extrapolation of NIST values above 7 mK, and a procedure described by Bremer *et al.* [55], the calculated T_A is 2.55 mK for melting pressure difference $P_A - P_{min} = 502,574$ Pa obtained in this work. This calculated T_A value is in good agreement with the T_A value determined in this experiment.

CHAPTER IV THERMODYNAMICS OF ORDERED SOLID ^3He

Introduction

In this chapter, the melting pressure measurements in various magnetic fields will be described, from which the magnetic phase diagram B - T will be obtained. The thermodynamic properties such as the spin wave velocity in the ordered phases, the entropy and the magnetization will be derived through the Clausius-Clapeyron equations. In addition various magnetic ordering transitions will be characterized.

The experimental setup was the same as that for the melting pressure thermometry experiment described in Chapter III, except that the ^{60}Co nuclear orientation thermometer and the tungsten fixed-point device were not installed. Actually this experiment was done before the melting pressure thermometry experiment and has been published [18,58,64]. The experimental setup was very similar to that used by Adams, Tang, and Uhlig [65] but with a number of significant improvements. A small compact magnet inside the vacuum was used to supply the magnetic field. This design would reduce the eddy-current heating in the melting pressure cell in the field and allow the zero field melting pressure cell in close proximity to the one in the field. The zero field melting pressure cell was welded to the same silver platform. This design is important because the transition temperatures in the fields can be measured relative to the one in the zero field. In this way, the magnetic phase diagram could be measured with very high precision. The larger cooling power of the nuclear demagnetization stage allowed smaller temperature drift. The better temperature control of the demagnetization stage helped to identify the HFP-PP transition to be discussed later.

In carrying out the experiment, the melting pressure versus Pt NMR temperature was first measured. To be consistent with the previous chapter, the Pt NMR calibration was against the new temperature scale, using the solid ordering at zero field $T_N=0.934$ mK as a calibration point. However, this slight T_N adjustment to Greywall's $T_N=0.931$ mK [6] (which was used in the Refs. [18,58,64]) was insignificant.

The melting pressure thermometry for $T>T_N$ and for $T<T_N$ can be represented by Eq. (3.4) and Eq. (3.5) respectively. Once the temperature scale was established, the melting pressure thermometer was used exclusively for obtaining the temperatures.

Magnetic Phase Diagram

The magnetic phase diagram was measured precisely in this experiment for fields below 0.653 T. At each field, the temperature was swept through the various phase transitions at a rate of 1-3 μ K per hour both on warming and cooling. The transition temperature on warming and cooling differed by 2 to 5 μ K due to the thermal gradient between ^3He and the cell body, and the average was used in the phase diagram. In some cases, the LFP-HFP transitions were determined by sweeping the field, since the phase line at lower temperatures was very flat. The field strength can be determined very accurately from the Pt NMR frequency through Eq. (2.15). Table 4.1 lists the various transition temperatures determined, where T_N , T_{LH} , and T_{HP} are the LFP-PP, LFP-HFP and HFP-PP transition temperatures, respectively.

For the LFP-PP or LFP-HFP transition, because of the latent heat, the time evolution of the melting pressure $P(t)$ leveled out for several hours in going through the transition. This is clear evidence for a first order transition. As will be discussed in detail later, the HFP-PP transition is also first order from the triple point T_t where the three phases meet, to about 0.65 T. The signature of the HFP-PP transition is different from either LFP-PP transition or LFP-HFP transition, since the plateau caused by the latent heat

is very slanted. The latent heat is easier to observe if the warming or cooling rate is small and if the heat exchanger couples well to the liquid. Otherwise the transition is smeared out, and looks like a second order transition. The slanted HFP-PP transition probably suggests the difficulty in heat transfer at this transition.

Table 4.1 Measured B - T coordinates for the magnetic phase diagram

T_N (mK)	B (T)	T_{LH} (mK)	B (T)	T_{HP} (T)	B (T)
0.934	0	0.849	0.395	0.855	0.395
0.931	0.075	0.838	0.4002	0.859	0.4002
0.929	0.1126	0.816	0.4077	0.867	0.4077
0.923	0.150	0.761	0.4206	0.903	0.450
0.912	0.200	0.703	0.4287	0.948	0.500
0.899	0.250	0.678	0.4335	0.984	0.549
0.884	0.300	0.652	0.4358	1.028	0.600
0.875	0.3287	0.537	0.4429	1.058	0.653
0.870	0.350	0.511	0.4443		
0.857	0.3832	0.476	0.4470		
0.850	0.3903	0.462	0.4483		

Before discussing the phase boundaries, brief thermodynamics governing the various quantities such as entropy S , magnetization M , molar volume V (extensive parameters) and temperature T , magnetic field B , and pressure P (intensive parameters) will be presented. Along a first-order transition which separates phase 1 and phase 2, these parameters are related by the Clausius-Clapeyron equation

$$\Delta S dT - \Delta V dP + \Delta M dB = 0, \quad \text{Eq. (4.1)}$$

where $\Delta S=S_2-S_1$, $\Delta V=V_2-V_1$, and $\Delta M=M_2-M_1$ are entropy, molar volume and magnetization differences, respectively. In a constant field, Eq. (4.1) reduces to the very well known Clausius-Clapeyron equation Eq. (1.1); for a fixed temperature, it becomes Eq. (1.2).

The solid ^3He molar volume changes between various magnetic phases were reported by Adams *et al.* [65] using the relation

$$\frac{\Delta V}{V} = \kappa_T \Delta P, \quad \text{Eq. (4.2)}$$

in an all solid ^3He experiment, where κ_T is the isothermal compressibility, ΔP is the solid ^3He pressure change at the transition. They found $\Delta V/V$ to be 9×10^{-5} for the PP-HFP transition, 5×10^{-5} for the HFP-LFP and 4×10^{-5} for the PP-HFP transition, all sufficiently small and can be ignored in Eq. (4.1). Therefore in discussing the ^3He magnetic phase diagram, the following magnetic Clausius-Clapeyron equation can be used

$$\frac{dT}{dB} = -\frac{\Delta M}{\Delta S}. \quad \text{Eq. (4.3)}$$

There are four special points in the phase diagram: the triple point (T, B) where all three phases coexist; the tricritical point (T_c, B_c) where the HFP-PP first order transition line extended from the triple point terminates and continues with a second order transition; the magnetic ordering transition in zero field $(T_M(0), 0)$; and the LFP-HFP transition at zero temperature $(0, B_{c1})$, obtained by extrapolation. The coordinates for these special points are listed in Table 4.2.

At $T=0$, according to the third law of thermodynamics, both entropies at the LFP and the HFP are zero, therefore $\Delta S=0$. From Eq. (4.3), the LFP-HFP transition line should be perpendicular to the B axis. Similarly, at $B=0$, there is no induced magnetization, i.e. $\Delta M=0$. From Eq. (4.3), the LFP-PP transition line should be perpendicular to the T axis.

Table 4.2. B - T coordinates for the special points

	T (mK)	B (T)
Triple point	0.850	0.392
Critical point	1.050	0.650
$T_N(0)$	0.934	0
B_{c1}	0	0.452

As will be discussed later, except for very near the HFP-PP transition, the entropies of both the LFP and the HFP have a T^3 functional form, characteristic of antiferromagnetic spin wave excitation with a linear dispersion relation. The magnetization discontinuity along this line is almost constant $\Delta M \approx \text{const}$, since B varies very little. From Eq. 4.3, the LFP-HFP transition line can be written as

$$B = 0.452 - 0.0965T^4, \quad \text{Eq. (4.4)}$$

where B is in tesla and T is in mK (the same for the following two equations).

The LFP-PP phase boundary can be represented quite well up to the triple point by the equation

$$T_N(B) = 0.934 - 0.543B^2. \quad \text{Eq. (4.5)}$$

This is expected if ΔM at the transition is proportional to B and there is little variation in ΔS (which is the case, as will be discussed later).

The HFP-PP transition line can be expressed by the empirical equation

$$B(T) = 0.304 - 0.813T + 1.08T^2. \quad \text{Eq. (4.6)}$$

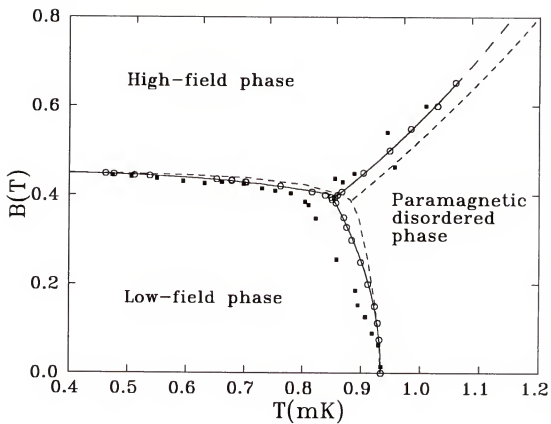


Figure 4.1 Magnetic phase diagram of solid ^3He measured in this work (open circles). Solid lines are from Eqs. (4.4), (4.5) and (4.6). Solid squares are from Osheroff [27]; dashed lines are from Greywall and Busch [63].

Figure 4.1 shows the measured phase diagram.

Order of the HFP-PP Transition

As mentioned in Chapter I, previous experimental results gave conflicting evidence on the nature of the HFP-PP transition. Kummer *et al.* [9], in their melting pressure measurements using a Pomeranchuk cell, found that there was no entropy discontinuity in the HFP-PP transition at 0.6 T or higher fields, in contrast to the case of the LFP-PP transition. Therefore the HFP-PP transition was second order. Prewitt and Goodkind [21], in their magnetization measurements showed that the HFP-PP transitions at 0.42 T and 0.5 T were very different from the LFP-PP transition. In cooling to the ordered phase, the magnetization changed abruptly at the LFP-PP transition. However, at the HFP-PP transition, the magnetization had a continuous change over about 100 μK temperature interval. Based on this the HFP-PP transition was concluded as second order.

In 1982, Osheroff [27] measured the NMR spectra of a solid ^3He sample grown inside a nylon mesh cylinder, surrounded by liquid ^3He . In a field of 0.44 T, he observed in the spectrum two well separated NMR peaks due to the different magnetizations from the HFP and the PP. By adjusting the liquid ^3He temperature to stabilize the HFP-PP interface, the NMR spectrum continued to show the above two peaks over a 4-hour period. Based on this, the HFP-PP transition at this field was probably first order, or at least very sharp.

These early experiments all had difficulty in controlling the temperature or might have thermal gradient in their samples; therefore, they could not give a definite answer to the nature of HFP-PP transition.

Meanwhile the theory did not do a very good job in predicting the order of the HFP-PP transition. The two- and three-parameter exchange models proposed by Roger *et al.* [33] produced a second-order phase-transition line separating the HFP and the PP. In

addition, within the HFP there was a first-order transition line extending from the triple point and ending at a critical point (see for example Figure 1.4). The existence of both first- and second-order transitions in the vicinity of that area could not be excluded by the experiment at that time. Cross and Fisher [66] raised three possibilities for the HFP-PP transition: (i) a first-order line becoming second order at a tricritical point and then extending up to high temperatures before bending back at $T=0$; (ii) a first-order line encircling the entire high field phase; and (iii) a first-order line ending at a critical point with no transition at higher fields, but instead with a Schottky-like entropy anomaly at high fields.

In 1986 Tang *et al.* [67] made an extensive study of the melting pressure in fields up to 0.495 T. By slowly sweeping up the temperature in the field of 0.400 T, both LFP-HFP and HFP-PP were observed. The melting pressure at the LFP-HFP transition leveled out for several hours, characteristic of a first-order transition, because of the latent heat. However just about 30 μK above the LFP-HFP transition, the HFP-PP transition did not show such a plateau. Based on this observation, they concluded that the HFP-PP transition was second order, shown in Figure 4.2.

It is easy to show that if the HFP-PP transition is first order, the magnetic phase diagram should have a kink at the triple point. In other words, the slopes of the LFP-PP transition and of the LFP-HFP transition are not continuous. Therefore measuring the B - T phase diagram should help us to identify the nature of the HFP-LFP transition. Unfortunately in earlier work, transition temperatures were not measured with enough accuracy to see the slope discontinuity.

Realizing this difficulty, Okamoto *et al.* [68] measured the transition melting pressure as a function of field near the triple point, since this did not require any accurate thermometers and both the field and the melting pressure could be measured with high resolution. In their B - P phase diagram they were able to show that the LFP boundary at

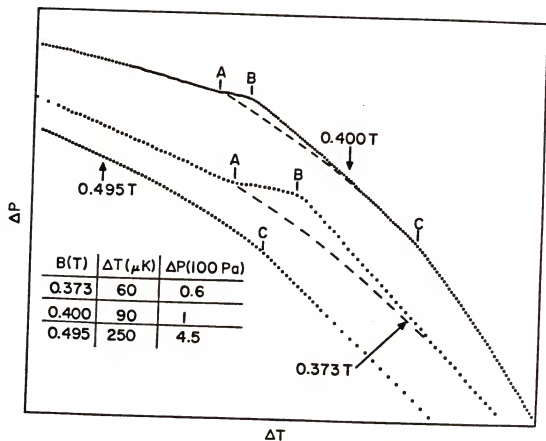


Figure 4.2 Melting pressure versus time or cell temperature for three fields studied by Tang *et al.* [65,67] Different scales are used for three fields, as shown in the table. C marks the HFP-PP transition; A-B is the latent heat section for the LFP-HFP transition ($B=0.400$ T) or for the LFP-PP transition ($B=0.373$ T).

the triple point had a very sharp turn, which strongly supported that the HFP-PP transition was first order in the vicinity of the triple point.

In this work we find that the HFP-PP transition is first order, but changes to second order at about 0.65 T. This conclusion will be presented from the following two perspectives.

Figure 4.3 shows the melting pressure versus the cell body temperature at $B=0.405\text{T}$ from 0.82 mK to 1.1 mK. The data were taken on a very slow warm up with the cells warming at a rate of $1.9\ \mu\text{K/h}$. At this field both LFP-HFP and HFP-PP transitions were seen. Similar to the observation of Tang *et al.* [67], the melting pressure at the LFP-HFP transition leveled out for 2 hours, because of the latent heat involved. However, the latent heat was clearly observed at the HFP-PP transition, much more profound than Tang *et al.* [67]. This is probably due to the better design of the cell and the slower warming rate made possible by the larger cooling power of the nuclear demagnetization stage (Tang *et al.* had $\approx 5\ \mu\text{K/h}$). Furthermore, on cooling the cell with a similar rate by a slow demagnetization of the PrNi₅ nuclear stage, the signature of the latent heat started at the same pressure (marked by the vertical arrow, see the inset). The melting pressure slope changed significantly after the transition over only about 20 μK temperature range. Therefore the transition at this field was first order.

As shown in Figure 4.3, the HFP-PP transition became broader as the field increased. At $B=0.653\ \text{T}$, the transition was very smooth, in contrast to the HFP-PP transitions at lower fields. One concern was that the smoothness of the HFP-PP transition in high field might be attributed to the thermal gradient caused by the field-dependent Kapitza resistance in the heat exchanger as suggested by Osheroff *et al.* [69]. The Kapitza resistance between the silver sinter and the liquid ^3He becomes significantly large in high fields. To avoid this problem, the melting pressure measurement at 0.653 T was taken in a cell whose heat exchanger was outside the field, as shown in Figure 4.4.

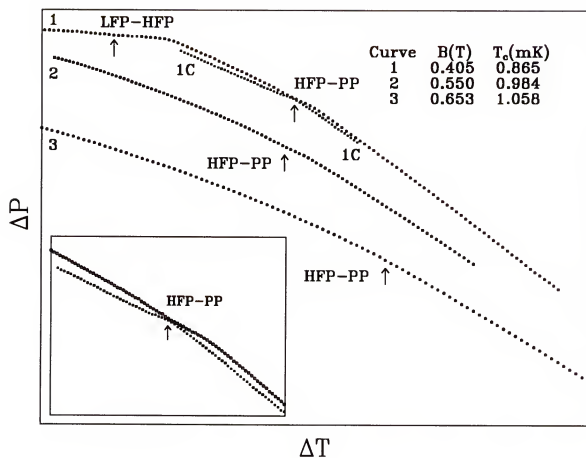


Figure 4.3 Melting pressure versus cell temperature in the vicinity of the magnetic phase transitions for various fields. The range of ΔP is 320 Pa and ΔT is 120 μK . The arrows mark the transitions. 1C is the cooling data. The inset shows the details near the HFP-PP transition at $B=0.405$ T, where ΔP is 60 Pa and ΔT is 25 μK .

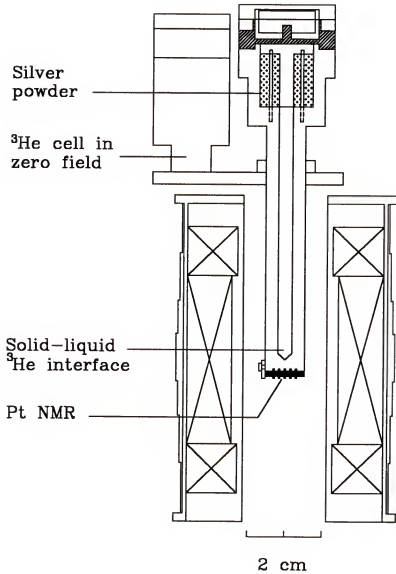


Figure 4.4 Experimental arrangement for melting pressure measurement at $B=0.653\text{T}$. The heat exchanger is located outside the magnet to reduce the field-dependent Kapitza resistance between silver powder and liquid ^3He .

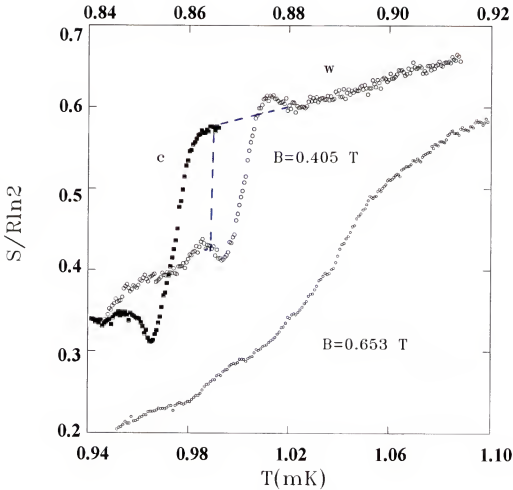


Figure 4.5 Entropy versus temperature through the HFP-PP transition at $B=0.405$ T and at $B=0.653$ T. For $B=0.405$ T (upper temperature scale), open circles are for warming (w) and the closed squares for cooling (c). For $B=0.653$ T (lower temperature scale), the transition is second order.

Figure 4.5 shows the entropy S versus temperature T near the HFP-PP transition at $B=0.405$ T and at $B=0.600$ T. The entropy was obtained through the Clausius-Clapeyron equation Eq. (1.1) and used a procedure described in the section of Entropy and Magnetization (to be described later). The HFP-PP transition at $B=0.405$ T is sharp and has a entropy discontinuity of about $0.18 R \ln 2$ over only about $20 \mu\text{K}$ temperature. In contrast, the HFP-PP transition at $B=0.653$ T is broad and the entropy has a continuous change over about $100 \mu\text{K}$ temperature range. Therefore the HFP-PP transition at this field is second order.

Figure 4.6 shows the entropy discontinuity ΔS over the HFP-PP transition as a function field. ΔS decreases as the field is increased and becomes zero at 0.65 T. Thus it is concluded that the HFP-PP transition is first order from the triple point to about 0.65 T and then continues as a second order transition at higher fields.

To enforce the conclusion that the HFP-PP transition is first order at low fields, Figure 4.7 shows the magnetic phase diagram in the B - P representation. The transition melting pressures are in reference to the zero field LFP-PP transition pressure $P_N(0)$. The horizontal axis is plotted as $P_N(0)-P$, reminiscent of the B - T phase diagram where the paramagnetic phase is at the right side. In this phase diagram, the LFP-PP transition line bends away from the LFP as the field increases. In other words, at the triple point the LFP-HFP transition line is not rounded into the LFP-PP transition line. Therefore there is a slope discontinuity at the triple point. In fact it was found that the slope dB/dP_N to be 4.8×10^{-4} T/Pa for the LFP-HFP line and -7.9×10^{-4} T/Pa for the LFP-PP line. Based on this, the HFP-PP transition near the triple point is first order.

Spin Wave Velocity in the Ordered Phases

In the ordered phases for $T \ll T_N$, the specific heat can be expressed as

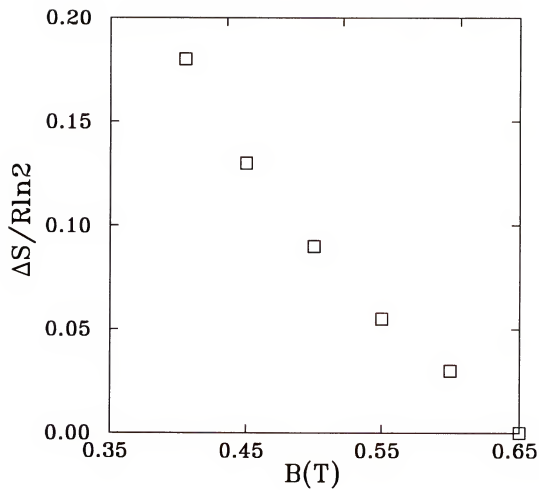


Figure 4.6 Entropy discontinuity ΔS over the HFP-PP transition as a function of field.

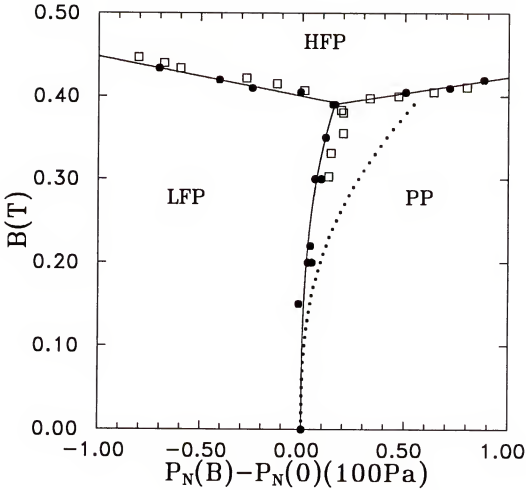


Figure 4.7 Magnetic phase diagram in the B - P representation. The melting pressures at transitions are relative to the solid ordering melting pressure in zero field $P_N(0)$. Closed circles are from this work, solid lines are guide to the eye. Open squares are from Okamoto *et al.* [68]. The dotted line is calculated from Greywall and Busch [63].

$$C_V = \frac{2n\pi^2V}{15} \left(\frac{k_B T}{V_{spin}\hbar} \right)^3, \quad \text{Eq. (4.7)}$$

where V is the solid molar volume, at the melting $V=24.22 \text{ cm}^3/\text{mole}$, V_{spin} the spin wave velocity averaged over all angles, n the number of spin-wave modes, k_B the Boltzmann constant and \hbar Plank's constant. This is because of the linear dispersion curve for the low-energy spin wave excitations. Neglecting the small specific heat of the liquid (less than 1% of the solid specific heat) the melting pressure is related to the specific heat of the solid by

$$C_V = -\Delta V T \frac{d^2 P}{dT^2}, \quad \text{Eq. (4.8)}$$

where ΔV is the molar volume change on melting. Therefore the melting pressure should be proportional to T^4 .

Figure 4.8 shows the melting pressure versus T^4 at several fields. In the LFP the T^4 temperature dependence continues up to the phase transitions. Notice that the slopes are independent of field within the experimental error. The melting pressure in the HFP deviates from the T^4 dependence near the HFP-PP transition and the slope decreases with increasing field.

In the region of the T^4 temperature dependence, the melting pressure as a function of B and T can be represented by

$$P(T, B) = P(0, B) - a(B)T^4, \quad \text{Eq. (4.9)}$$

where $P(0, B)$ is the limiting melting pressure at $T=0$. Using Eqs. (4.7) and (4.8), the spin wave velocity can be written in terms of $a(B)$ as

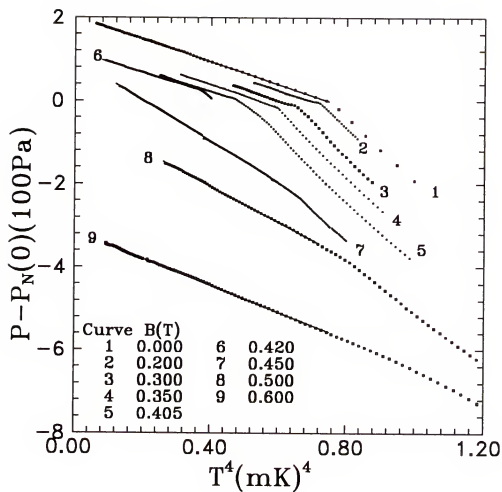


Figure 4.8 Melting pressure versus T^4 in several fields. The pressures are relative to the solid ordering melting pressure in zero field $P_M(0)$.

$$V_{spin} = \left(\frac{n\pi^2 k_B^4 V}{90\alpha(B)\Delta V \hbar^3} \right), \quad \text{Eq. (4.10)}$$

where the number of spin-wave modes in the LFP $n=2$, and $n=1$ in the HFP.

Figure 4.9 shows the spin-wave velocity as a function of field obtained from Eq. (4.10). Within the experimental error, the spin wave velocity, V_{spin} is independent of field in the LFP. This is in contrast to the calculations of Greywall and Busch [63], based on scaling of the heat capacity with field in the HFP and an assumed value of the triple point temperature, $T_T=0.883 \mu\text{K}$ (normalized to $T_N = 0.934 \text{ mK}$) which is considerable higher than $0.850 \mu\text{K}$ determined in this experiment. The points shown by the circles are derived from the results of Osheroff *et al.* [19]. These values are given in Ref. [63], but have not been reported in the original literature. In the HFP, V_{spin} increases with field and there is generally good agreement among various authors. As will be discussed later, the significance of field-independent spin-wave velocity in the LFP is that the magnetization is temperature independent.

Entropy and Magnetization

Figure 4.10 shows the raw data of melting pressure as function of temperature at various fields. These data cover much wider temperature range than those in the careful studies of HFP-PP transition described in the section of Order of the HFP-PP transition. Data were taken on warming by the heat leak of a few nano watt and the warming rate was 2-7 μK per hour. The temperatures $T(t)$ were converted from the melting pressure at zero field, using the scale established in chapter III. Except at the transitions where the temperature of ^3He was held by the latent heat, the cell temperature $T(t)$ and ^3He temperature differed only a few μK .

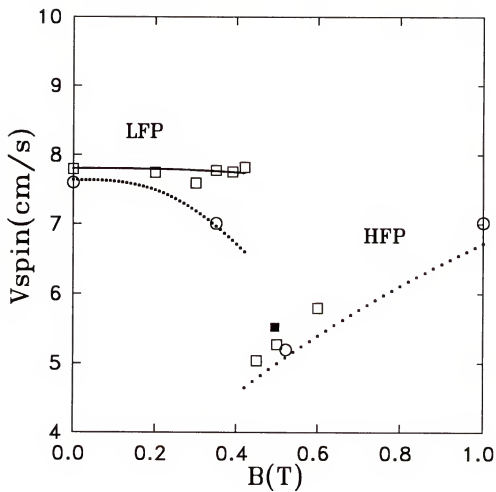


Figure 4.9 Spin-wave velocity as function of field. Open circles are from Osheroff *et al.* [19], the dotted lines are from Greywall and Busch [63], solid square is from Tang *et al.* [67], open squares are measured in this work and solid line is guide to the eye.

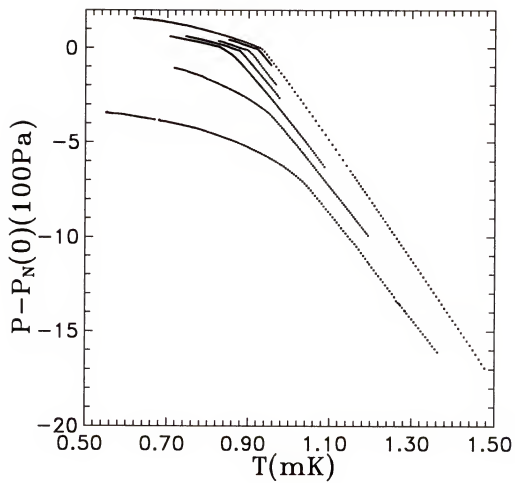


Figure 4.10 Melting pressure as function of temperature P - T at various fields. From top to bottom, the curves are 0.0 T, 0.2 T, 0.3 T, 0.35 T, 0.405 T, 0.5 T and 0.6 T.

The entropy of the solid, obtained from dP/dT through the Clausius-Clapeyron equation using $\Delta V=1.314 \text{ cm}^3/\text{mole}$ and $S_l \approx 0$, is shown Figure 4.11 for various fields. The melting pressure derivative dP/dT was programmed by the following procedure:

$$\frac{dP}{dT} \left(i + \frac{n}{2} \right) = \frac{P(n+i) - P(i)}{T(n+i) - T(i)}, \quad \text{Eq. (4.11)}$$

where i is the i -th data point, n was taken such that $\Delta T=T(n+i)-T(i)$ is about $15 \mu\text{K}$. In the region of the latent heat the melting pressure changes very little and the derivative shows an artificial behavior because of this procedure, which should be ignored.

In the region of T^4 dependence of the melting pressure, the entropy has a T^3 dependence, which can be written as

$$S(T, B) = 4a(B)\Delta VT^3. \quad \text{Eq. (4.12)}$$

In the LFP, as demonstrated by the plot of P versus T^4 in Figure 4.8, $a(B) \approx a_0$. Therefore the entropy is essentially field independent. The entropy in the HFP can still be represented by Eq. (4.12), except very near the HFP-PP transition where it rises more rapidly than T^3 . In contrast to the LFP, $a(B)$ is a function of field, the entropy has a strong field dependence, consistent with the temperature dependence of the magnetization, to be discussed later.

In the PP, for $T < 3 \text{ mK}$, the entropy can be represented quite well by

$$S(T, B) = S(T, 0) - \frac{bR \ln 2}{2} \left(\frac{B}{T} \right)^2, \quad \text{Eq. (4.13)}$$

where $b=0.58 \text{ (mK/T)}^2$, R is the gas constant and $S(T, 0)$ is the entropy at zero field. This is consistent with the Curie-law behavior of the magnetization, given by

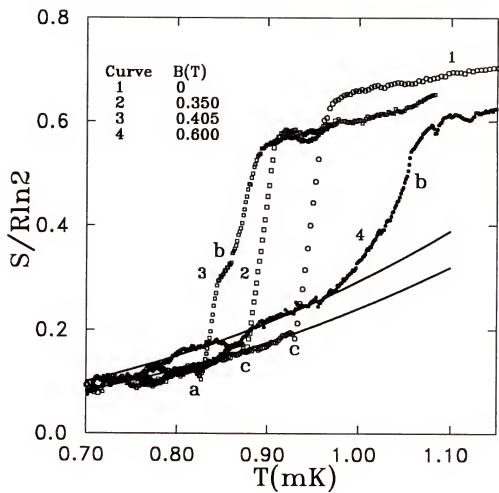


Figure 4.11 Entropy versus temperature for various fields studied. The solid lines are T^4 fits. *a* is the LFP-HFP transition; *b* is the HFP-PP transition and *c* is the LFP-PP transition.

$$M(T) = b \left(\frac{B}{T} \right) R \ln 2, \quad \text{Eq. (4.14)}$$

which has been observed by a number of workers [14,21,63]. Eq. (4.14) is obtained through the Maxwell relation

$$\left(\frac{\partial M}{\partial T} \right)_B = \left(\frac{\partial S}{\partial B} \right)_T. \quad \text{Eq. (4.15)}$$

Figure 4.12 shows the family of entropy curves based on the discussions above.

The field dependence of the entropy discontinuity across the LFP-PP transition is shown in Figure 4.13. The entropy discontinuity shows a very weak field dependence, primary because of the lack of B dependence of S in the LFP. The dashed line calculated by Greywall and Busch [63] and the measurements of Tang *et al.* [67] show a much stronger field dependence. Both these results are probably in error. The results of Greywall and Busch are based on a triple point temperature, which is considerable higher than the value determined in this experiment. The measurements of Tang *et al.* had difficulty in the temperature determination. In their experimental arrangement, there was no zero field melting pressure cell. Therefore in calibrating their Pt NMR thermometer, they had to warm up to the superfluid ^3He A transition temperature T_A .

The temperature dependence of the magnetization is related to the field dependence of the entropy through the Maxwell relation Eq. (4.15). In the LFP or HFP where the T^4 temperature dependence of the melting pressure is valid the magnetization can be expressed as

$$M(T, B) = M(0, B) + \Delta V T^4 \left[\frac{da(B)}{dB} \right], \quad \text{Eq. (4.16)}$$

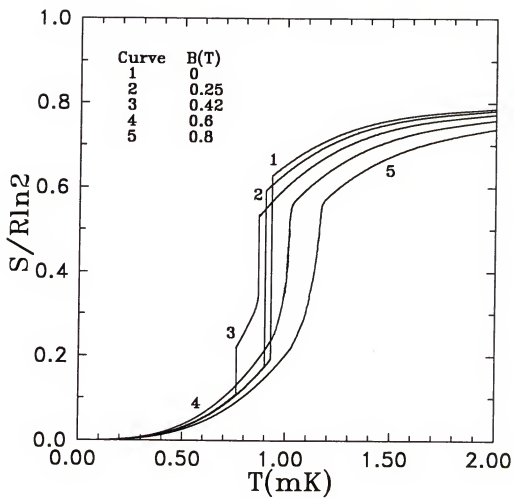


Figure 4.12 Family of entropy versus temperature curves.

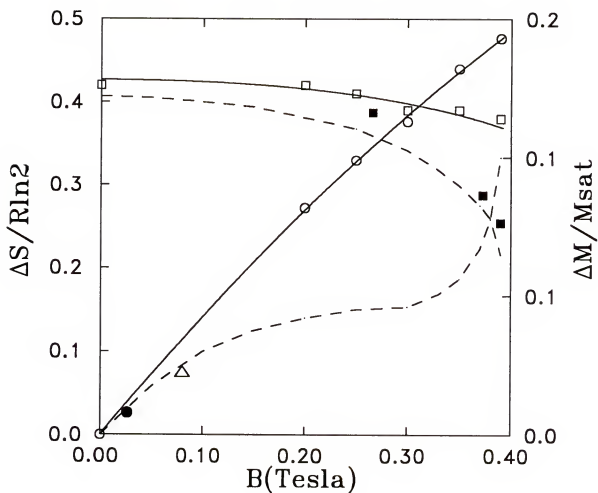


Figure 4.13 Entropy and magnetization discontinuity (ΔS , $\Delta M/M_{sat}$) across the LFP-PP transition. Open squares (ΔS) and circles ($\Delta M/M_{sat}$) are from this work, solid lines are fits to the data. Closed squares are from Tang *et al.* [67], dashed lines are from Greywall and Busch [63], solid circle is from Hata *et al.* [14], open triangle is from Prewitt and Goodkind. [21].

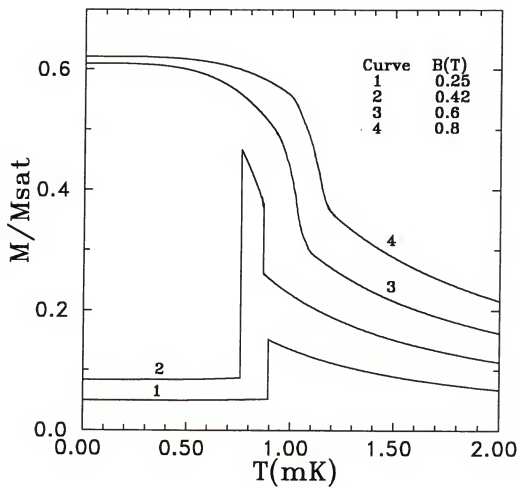


Figure 4.14 Family of magnetization versus temperature curves.

where $M(0,B)$ is the magnetization at $T=0$, which can be obtained from the limiting melting pressure $P(0,B)$ by

$$M(0,B) = -\Delta V \frac{dP(0,B)}{dB}. \quad \text{Eq. (4.17)}$$

Here the magnetization of liquid ^3He is ignored, since it is only <1% of the magnetization of solid ^3He . The magnetic susceptibility χ is the derivative of $M(0,B)$ with respect to B

$$\chi = -\Delta V \frac{d^2 P(0,B)}{dB^2}. \quad \text{Eq. (4.18)}$$

In the LFP, $\chi=1.3 \times 10^{-4}$ /mole, obtained from this work, is in good agreement with Osheroff *et al.* [19] who also calculated it from the field depression of the melting pressure $P(T,B)$. Although they did not have a reliable thermometer to extrapolate the melting pressure to get $P(0,B)$, the melting pressure below 0.4 mK is essentially the same as $P(0,B)$. Since $\alpha(B)$ was found to be field independent, Eq. (4.16) shows that $M(T,B)$ is temperature independent. This important result is in contrast to the conclusion of Greywall and Busch [63] that raising the temperature in the LFP would increase the magnetization.

In the HFP, a high magnetization ($>0.5 M_{\text{sat}}$) was found. In general $\alpha(B)$ decreases as field increases and therefore according to Eq. (4.16), the magnetization is a function of temperature. Figure 4.13 shows a family of magnetization curves based on the above discussions. In the HFP, $\chi(B)$ is taken from Osheroff *et al.* [19], since it is obtained using a much wider range of field.

Solid ^3He Molar Volume at Melting Below 1mK

An interesting conclusion that can be drawn from this work is that the molar volume curve V - T of solid ^3He has a minimum (kink) at the ordering temperature

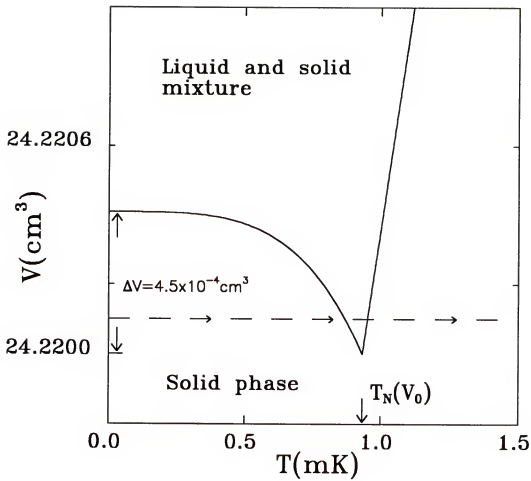


Figure 4.15 Molar volume V versus T near 1 mK. There is a very shallow minimum at $T = T_N(V_0)$, where $V_0 = 24.22 \text{ cm}^3/\text{mole}$, the molar volume at melting.

$T_N(V_0)=0.934$ mK, as shown in Figure 4.15. Here $V_0=24.22$ cm³/mole is the molar volume at melting. The following discussions are based on $B=0$.

As has been discussed in the section on Spin-wave velocity in the ordered phases, the melting pressure in the ordered phase (LFP) is proportional to the T^4 , expressed by Eq. (4.9). The isochoric pressure of solid ³He is also proportional to the T^4 in the ordered phase, which is not so trivial. The following is the analysis.

The entropy is assumed to scale with the molar volume V in following way

$$S(V, T) = f\left(\frac{T}{T_N(V)}\right), \quad \text{Eq. (4.19)}$$

where $T_N(V)$ is the ordering temperature at the molar volume V expressed by

$$T_N(V) = T_N(V_0) \left(\frac{V}{V_0}\right)^\gamma, \quad \text{Eq. (4.20)}$$

where $\gamma=16.5$ from Hata *et al.*[14]. Taking the derivative of $S(V, T)$ with respect to V and using Eq. (4.20), it is easy to show that

$$\left(\frac{\partial S}{\partial V}\right)_T = -\frac{\gamma T}{T_N(V)} f' \left[\frac{T}{T_N(V)} \right] \frac{1}{V}. \quad \text{Eq. (4.21)}$$

In the ordered phase, the entropy can be expressed as

$$S(V, T) = a \left[\frac{T}{T_N(V)} \right]^3, \quad \text{Eq. (4.22)}$$

where α is a constant which has the same unit as the gas constant R . This is expected from the spin-wave theory and can be obtained from the specific heat expressed in Eq. (4.7). At the melting molar volume V_0 , $\alpha=0.19R\ln 2$ from this work. Using Eq. (4.21), the entropy derivative with respect to the molar volume is

$$\left(\frac{\partial S}{\partial V}\right)_T = -3\alpha\gamma \left[\frac{T}{T_N(V)}\right]^3 \frac{1}{V}. \quad \text{Eq. (4.23)}$$

The isochoric pressure slope is obtained through the Maxwell relation

$$\left(\frac{\partial P}{\partial T}\right)_V = \left(\frac{\partial S}{\partial V}\right)_T, \quad \text{Eq. (4.24)}$$

therefore,

$$\left(\frac{\partial P}{\partial T}\right)_V = -3\alpha\gamma \left[\frac{T}{T_N(V)}\right]^3 \frac{1}{V}. \quad \text{Eq. (4.25)}$$

The isochoric pressure is obtained by integrating over T on both sides of Eq. (4.25)

$$P(T,V) = P(0,V) - \frac{3\alpha\gamma}{4V[T_N(V)]^3} T^4. \quad \text{Eq. (4.26)}$$

Here $P(0,V)$ is the isochoric pressure at $T=0$, which can be related to the limiting melting pressure $P(0,V_0)$ through the isothermal compressibility

$$\kappa_T = -\frac{1}{V} \left(\frac{\partial V}{\partial P}\right)_T. \quad \text{Eq. (4.27)}$$

Eq. (4.26) thus can be written in the following form

$$P(T, V) = P(0, V_0) + \frac{1}{\kappa_T} \ln\left(\frac{V_0}{V}\right) - \frac{3\alpha\gamma}{4V[T_N(V)]^3} T^4. \quad \text{Eq. (4.28)}$$

The melting pressure is obtained through Clausius-Clapeyron equation

$$\frac{dP}{dT} = -\frac{S(V_0, T)}{\Delta V}, \quad \text{Eq. (4.29)}$$

where the liquid ^3He entropy is ignored and $\Delta V = 1.314 \text{ cm}^3$ is the molar volume change on melting (here the small variation of ΔV with T has been ignored). By integrating Eq. (4.29) and using the entropy in Eq. (4.22), the melting pressure is

$$P(T, V_0) = P(0, V_0) - \frac{\alpha}{4\Delta V[T_N(V_0)]^3} T^4. \quad \text{Eq. (4.30)}$$

The ratio of the isochoric pressure slope and the melting pressure slope is

$$\frac{3\gamma\Delta V}{V} \left[\frac{T_N(V_0)}{T_N(V)} \right]^3. \quad \text{Eq. (4.31)}$$

At the melting molar volume $V=V_0$, the result is 2.69.

Thus, for a total solid ^3He sample slightly below the melting molar volume $V=V_0$, the pressure decreases with increasing T faster than the melting pressure. At some temperature $0 < T < T_N(V_0)$, the solid starts to melt, as shown in Figure 4.16. This can happen only if there is a molar volume minimum as shown in Figure 4.15. The molar volume curve $V-T$ has a minimum at $T=T_N(V_0)$ and the slope has a discontinuity. However, the molar volume minimum is very shallow and can be evaluated.

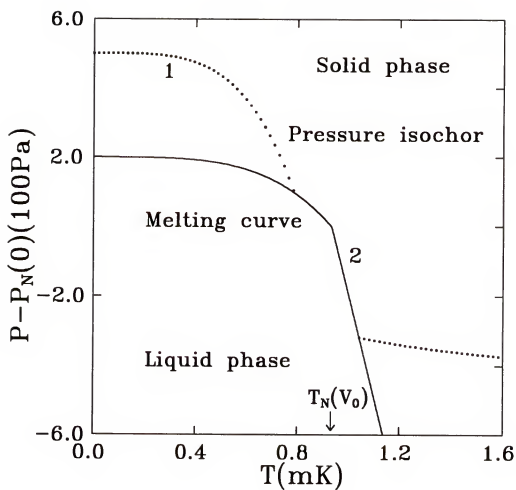


Figure 4.16 The isochoric pressure decreases with T faster than the melting pressure. At some $0 < T < T_N(V_0)$, the solid melts and enters to the solid phase again at $T > T_N(V_0)$.

The molar volume change can be expressed by

$$dV = \left(\frac{\partial V}{\partial P} \right)_T dP + \left(\frac{\partial V}{\partial T} \right)_P dT. \quad \text{Eq. (4.32)}$$

The first term on the right side of Eq. (4.32) is related to the isothermal compressibility κ_T , and the second term can be expressed in terms of thermal expansion coefficient

$$\alpha = \frac{1}{V} \left(\frac{\partial V}{\partial T} \right)_P = \kappa_T \left(\frac{\partial P}{\partial T} \right)_V. \quad \text{Eq. (4.33)}$$

Using the Maxwell relation Eq. (4.24), the molar volume slope is

$$\frac{dV}{dT} = V \kappa_T \left[\left(\frac{\partial S}{\partial V} \right)_T - \frac{dP}{dT} \right]. \quad \text{Eq. (4.34)}$$

On the melting curve, $V=V_0$ and for $T < T_N(V_0)$, use the result of Eq. (4.23) for $(\partial S / \partial V)_T$ and Eq. (4.29) for dP / dT ,

$$\frac{dV}{dT} = \kappa_T \alpha \left(-3\gamma + \frac{V_0}{\Delta V} \right) \left[\frac{T}{T_N(V_0)} \right]^3. \quad \text{Eq. (4.35)}$$

Where the approximation $V \approx V_0$ has been made since the variation of $V(T)$ is small. Use $\kappa_T = 5.1 \times 10^{-8} \text{ Pa}^{-1}$ from Halperin *et al.* [3], $\alpha = 0.19 R \ln 2$ from this work ($R = 8.314 \text{ J/Kmole}$), $\gamma = 16.5$ from Hata *et al.* [14] and $V_0 / \Delta V = 24.22 / 1.314$, the result is

$$\frac{dV}{dT} = -1.73 \times 10^{-3} \left[\frac{T}{T_N(V_0)} \right]^3 \text{ cm}^3 (\text{mK mole})^{-1}. \quad \text{Eq. (4.36)}$$

The slope is negative and the molar volume difference $V(T)-V(0)$ for $0 < T < T_N(V_0)$ is obtained by integrating the above equation

$$V(T) - V(0) = -0.43 \times 10^{-3} \frac{T^4}{T_N^3(V_0)} \text{ cm}^3(\text{mK mole})^{-1}, \quad \text{Eq. (4.37)}$$

The molar volume difference between $T=0$ and $T=T_N(V_0)$ is $V(T_N)-V(0)=-4.5 \times 10^{-4} \text{ cm}^3$.

By using the entropy data above $T_N(V_0)$ (see Figure 4.12), at $V=V_0$ and slightly above the ordering temperature $T_N(V_0)$, $(\partial S / \partial V)_T = 6.24R \ln 2$ and $(dP / dT) = 11.5R \ln 2$, obtained from Eqs. (4.21) and (4.29), respectively. The molar volume slope obtained from Eq. (4.34) is $dV / dT = 1.5 \times 10^{-3} \text{ cm}^3 / (\text{mK mole})$. It is positive, therefore the molar volume curve $V-T$ at $T=T_N(V_0)$ has a minimum with a discontinuous slope.

Since the molar volume change at melting is $\Delta V = 1.314 \text{ cm}^3$, the small variation in $V(T)$ below $T_N(V_0)$ given by Eq. (4.37) would be quite difficult to detect. However, the change in slope for an all solid sample intersecting the melting curve as shown in Figure 4.16 should be readily detectable in the experiment.

Conclusions

In this Chapter, the melting pressure in several magnetic fields were measured, from which a precise magnetic phase diagram $B-T$ was obtained. The transition from the LFP to either the PP or the HFP is first order. The HFP-PP transition is identified as first order from the triple point of the phase diagram to about 0.65 T, and continues with a second-order transition at high fields. In the LFP, the melting pressure has a T^4 temperature dependence up to the phase transitions, characteristic of antiferromagnetic spin waves with a linear dispersion relation. The spin wave velocity is 7.8 cm/s, independent of field. The magnetization is temperature independent and can be described by a constant susceptibility. The melting pressure in the HFP deviates from the T^4

dependence near the HFP-PP transition, resulting in a very rapid entropy change near T_c . The spin wave velocity increases with field, consistent with a temperature-dependent magnetization. The entropy and magnetization discontinuities across the HFP-PP and LFP-PP transitions have been determined. The molar volume exhibits a very shallow minimum at the ordering transition T_N .

APPENDIX

Solid angle correction

In the actual γ -ray measurement, the radiation is detected over the solid angle extended by the detector; the solid angle corrections Q_2 and Q_4 are needed in Eq. (2.16). An extensive tabulation of Q_k are already calculated for NaI detectors [70]. Q_k for germanium detectors are calculated differently [71]. The solid angle corrections for this work have to be calculated according to this particular situation. The calculated solid angle corrections are $Q_2=0.9946$ and $Q_4=0.9821$. The calculation is briefly described here.

Table A1. γ -ray absorption coefficient

γ -ray energy (MeV)	Absorption coefficient τ (cm ⁻¹)	γ -ray energy (MeV)	Absorption coefficient τ (cm ⁻¹)
0.03	70.6	0.3	0.196
0.05	17.0	0.5	0.0517
0.1	2.59	1.0	0.00927
0.15	0.982	1.5	0.00382
0.2	0.521		

Following the method of Rose [72], the solid angle correction factors are expressed as

$$Q_k(\gamma) = \frac{J_k(\gamma)}{J_0(\gamma)}, \quad (\text{A1})$$

where

$$J_k(\gamma) = \int P_k(\cos\beta)(1 - e^{-\tau(\gamma)x(\beta)}) \sin\beta d\beta. \quad (\text{A2})$$

The integration is carried out over the path length $x(\beta)$ through the active volume of the detector, shown in Figure A1. The integration variable β is the angle between the γ -ray propagation direction and the detector symmetry axis. $\tau(\gamma)$ is the γ -ray absorption coefficients listed in Table A.1 taken from Ref. [72].

Here the integration is divided into three region:

$$1). \tan^{-1}\left(\frac{r}{D+L}\right) \leq \beta \leq \tan^{-1}\left(\frac{r}{D}\right),$$

$$x(\beta) = \frac{D+L}{\cos\beta} - \frac{r}{\sin\beta}; \quad \text{Eq. (A3)}$$

$$2). \tan^{-1}\left(\frac{r}{D}\right) \leq \beta \leq \tan^{-1}\left(\frac{R}{D+L}\right),$$

$$x(\beta) = \frac{L}{\cos\beta}; \quad \text{Eq. (A4)}$$

$$3). \tan^{-1}\left(\frac{R}{D+L}\right) \leq \beta \leq \tan^{-1}\left(\frac{R}{D}\right),$$

$$x(\beta) = \frac{R}{\sin\beta} - \frac{D}{\cos\beta}; \quad \text{Eq. (A5)}$$

Figure A2 shows the computed solid angle correction factors Q_k as a function of source to detector distance D for this detector parameters $R=2.00$ cm, $r=0.3$ cm, $L=3.5$ cm and $\gamma=0.00846$ cm⁻¹, for the averaged ⁶⁰Co γ -ray energy 1.25 MeV.

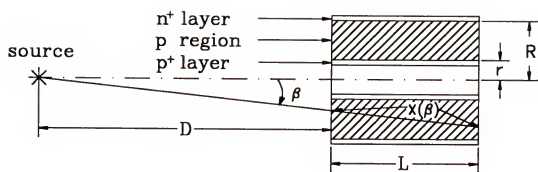


Figure A1 Geometry of source-detector configuration for the calculation of solid angle corrections in a coaxial germanium detector.

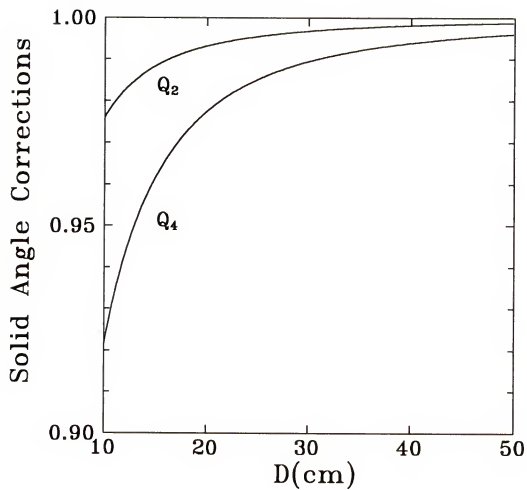


Figure A2 Calculated solid angle correction factors Q_k as function of source to detector distance D for the germanium detector used in the experiment.

REFERENCES

1. E. D. Adams, Gordon Research Conference, Crystal Mountain, WA, July 1967 (unpublished).
2. R. A. Scribner and E. D. Adams, in *Temperature, Its Measurement and Control in Science and Industry*, edited by H. H. Plumb (Instrument Society of America, Pittsburg, 1972), vol. 4, part 1, p.37.
3. W. P. Halperin, F. B. Rasmussen, C. N. Archie, and R. C. Richardson, *J. Low Temp. Phys.* **31**, 617 (1978).
4. D. S. Greywall, *Phys. Rev.* **B 31**, 2675 (1985).
5. J. H. Colwell, W. E. Fogle, and R. J. Soulen, Jr., in *Proceedings of the 17th International Conference on Low Temperature Physics*, edited by U. Eckern, A. Schmid, W. Weber, and H. Wuhl (North-Holland, Amsterdam, 1984), part1, p. 395.
6. D. S. Greywall, *Phys. Rev.* **B 33**, 7520 (1986).
7. H. Fukuyama, H. Ishimoto, T. Tazaki, and S. Ogawa, *Phys. Rev.* **B 36**, 8921 (1987).
8. W. E. Fogle, R. J. Soulen, Jr. and J. H. Colwell, in *Temperature, Its Measurement and Control in Science and Industry*, vol. 6. (Am. Inst. Phys., New York, 1992), edited by J. F. Schooley, p. 91.
9. R. B. Kummer, R. M. Muller, and E. D. Adams, *J. Low Temp. Phys.* **27**, 319 (1977).
10. E. D. Adams, *Can. J. Phys.* **65**, 1336 (1987).
11. J. L. Baum, D. F. Brewer, J. G. Daunt, and D. O. Edwards, *Phys. Rev. Lett.* **3**, 127 (1959).
12. E. R. Grilly, *J. Low Temp. Phys.* **4**, 1626 (1971).
13. G. C. Straty and E. D. Adams, *Phys. Rev.* **150**, 123 (1966).
14. T. Hata, S. Yamasaki, T. Kodama, and T. Shigi, *J. Low Temp. Phys.*, **71**, 193 (1988).

15. Y. Takano, N. Nishida, Y. Miura, H. Fukuyama, H. Ishimoto, and S. Ogawa, *Phys. Rev. Lett.* **55**, 1490 (1985).
16. H. Yano, H. Kondo, T. Suzuki, Y. Minamide, T. Kato, Y. Miura, and T. Mamiya, *Phys. Rev. Lett.* **65**, 3401 (1990).
17. T. Okamoto, H. Fukuyama, H. Akimoto, H. Ishimoto, and S. Ogawa, *Phys. Rev. Lett.* **72**, 868 (1994).
18. J. S. Xia, W. Ni, and E. D. Adams, *Phys. Rev. Lett.* **70**, 1481 (1993).
19. D. D. Osheroff, H. Godfrin, and R. R. Ruel, *Phys. Rev. Lett.* **58**, 2458 (1987).
20. D. D. Osheroff and C. Yu, *Phys. Lett.* **77A**, 458 (1980).
21. T. C. Prewitt and J. M. Goodkind, *Phys. Rev. Lett.* **44**, 1699 (1980).
22. H. Fukuyama, T. Fukuda, T. Okamoto, H. Akimoto, H. Ishimoto, and S. Ogawa, *Physica B*, **169**, 197 (1991).
23. J. H. Hetherington, *Physica* **108B**, 855 (1982).
24. E. D. Adams, E. A. Schuberth, G. E. Haas, and D. M. Bakalyar, *Phys. Rev. Lett.* **44**, 789 (1980).
25. D. D. Osheroff, M. C. Cross, and D. S. Fisher, *Phys. Rev. Lett.* **44**, 792 (1980).
26. A. Benoit, J. Bossy, J. Flouquet, and J. Schweizer, *J. Phys. Lett.* **46**, L923 (1985).
27. D. D. Osheroff, *Physica B+C*, **109**, 1461 (1982).
28. Y. P. Feng, P. Schiffer, and D. D. Osheroff, *Phys. Rev. Lett.* **67**, 691 (1991).
29. W. P. Kirk and E. D. Adams, *Phys. Rev. Lett.* **27**, 392 (1971).
30. T. Prewitt and J. M. Goodkind, *Phys. Rev. Lett.* **39**, 1283 (1977).
31. F. D. C. Willard, *La Recherche* **11**, 972 (1980).
32. J. H. Hetherington and F. D. C. Willard, *Phys. Rev. Lett.* **35**, 1442 (1975).
33. M. Roger, J. H. Hetherington, and J. M. Delrieu, *Rev. Mod. Phys.* **55**, 1 (1983).
34. H. L. Stipdonk and J. H. Hetherington, *Phys. Rev.* **B 31**, 4684 (1985).

35. D. M. Ceperley and G. Jacucci, *Phys. Rev. Lett.* **58**, 1648 (1987).
36. H. Godfrin and D. D. Osheroff, *Phys. Rev. B* **38**, 4492 (1988).
37. P. M. Berglund, H. K. Collan, G. J. Ehnholm, R. G. Gylling, and O. V. Lounasmaa, *J. Low Temp. Phys.* **6**, 357 (1972).
38. R. J. Soulen Jr. and H. Marshak, *Cryogenics* **22**, 408 (1980).
39. H. Marshak, *J. Res. NBS* **88**, 175 (1983).
40. H. Marshak, in *Low-Temperature Nuclear Orientation*, edited by N. J. Stone and H. Postma, (North-Holland, Amsterdam, 1986).
41. Y. Takano, *Rev. Sci. Instrum.* **65**, 5 (1994).
42. M. Kubota, H. R. Folle, Ch. Buchal, R. M. Muller, and F. Pobell, *Phys. Rev. Lett.* **45**, 1812 (1980).
43. G. C. Straty and E. D. Adams, *Rev. Sci. Instrum.* **40**, 1393 (1969).
44. E. D. Adams, *Rev. Sci. Instrum.* **64**, 601 (1993).
45. E. D. Adams, K. Uhlig, Y. Tang and G. E. Haas, *Phys. Rev. Lett.*, **52**, 2249 (1984).
46. F. Pobell, in *Matters and Methods at Low Temperatures* (Spring-Verlag).
47. R. J. Soulen, Jr. and R. B. Dove, NBS special publication **260-62**, U. S. Government Printing Office.
48. N. W. Ashcroft and N. D. Mermin, in *Solid State Physics* (Saunders College).
49. J. Bardeen, L. N. Cooper, and J. R. Schrieffer, *Phys. Rev.* **108**, 1175 (1975).
50. V. L. Ginsburg and L. D. Landau, *Zh. Eksperim. i Teor. Fiz.* **20**, 1064 (1950).
51. G. W. Swift and D. S. Buchanan, in *Proceedings of the 18th International Conference on Low Temperature Physics* [Jpn J. Appl. Phys. **26-3**, 1828(1987)].
52. P. Schiffer, M. T. O'Keefe, M. D. Hildreth, H. Fukuyama, and D. D. Osheroff, *Phys. Rev. Lett.* **69**, 120 (1992).
53. A. J. Leggett, *Phys. Rev. Lett.* **53**, 1096 (1984), *Phys. Rev. Lett.* **54**, 246 (1985).
54. J. C. Wheatley, *Rev. Mod. Phys.* **47**, 415 (1975).

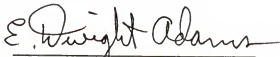
55. J. Bremer and M. Durieux, in *Temperature, Its Measurement and Control in Science and Industry*, vol. 6. (Am. Inst. Phys., New York, 1992), edited by J. F. Schooley, p. 16.
56. O. Avenel, M. Bernier, D. Bloyet, P. Piejus, E. Varaquaux, and C. Vibet, in *Proceedings of the 14th International Conference on Low Temperature Physics*, edited by M. Krusius and M. Vuorio (North-Holland, Amsterdam, 1975), vol. 4, p. 64.
57. A. Hoffman, J. Engert, and W. Buck, *Physica B* **194-196**, 19 (1994).
58. W. Ni, J. S. Xia, and E. D. Adams, *Phys. Rev. B*, **50** (1994).
59. D. N. Paulson, M. Krusius, and J. C. Wheatley, *J. Low Temp. Phys.* **34**, 63 (1979).
60. T. A. Alvesalo, T. Haavasoja, and M. T. Manninen, *J. Low Temp. Phys.* **45**, 373 (1981); **36**, 712 (E) (1979).
61. J. C. Wheatley, *Physica* **69**, 218 (1973).
62. A. I. Ahonen, M. Krusius, and M. A. Paalanen, *J. Low Temp. Phys.* **25**, 421 (1976).
63. D. S. Greywall and P. A. Busch, *Phys. Rev. B* **36**, 6853 (1987).
64. J. S. Xia, W. Ni, and E. D. Adams, *J. Low Temp. Phys.* **89**, 355 (1992).
65. E. D. Adams, Y. H. Tang, and K. Uhlig, *J. Low Temp. Phys.* **84**, 109 (1991).
66. M. C. Cross and D. S. Fisher, *Rev. Mod. Phys.* **57**, 881 (1985).
67. Y. H. Tang, E. D. Adams, and K. Uhlig, *Phys. Rev. Lett.* **57**, 222 (1986).
68. T. Okamoto, H. Fukuyama, T. Fukuda, H. Ishimoto, and S. Ogawa, *Physica B* **165&166**, 825 (1990).
69. D. D. Osheroff and R. C. Richardson, *Phys. Rev. Lett.* **54**, 1178 (1985).
70. M. J. Yates, in *Perturbed Angular Corrections*, edited by E. Karlsson, E. Matthias, and K. Siegbahn (North-Holland, Amsterdam, 1964), p. 453.
71. K. S. Krane, *Nucl. Instru. Meth.* **98**, 205 (1972).
72. M. E. Ross, *Phys. Rev.* **91**, 610 (1953).

BIOGRAPHICAL SKETCH

Wenhai Ni was born on July 23, 1963, in Hangzhou, Zhejiang Province, People's Republic of China, as the youngest son of Tieqi Ni and Yinnan Shen. As an honored high school student he was admitted to the University of Science and Technology of China, Hefei, Anhui Province, through the standard national entrance examinations. Soon after he graduated there, he accepted an offer to the master's program in the Department of Physics, University of Puerto Rico, Rio Piedras, where he was awarded a M. S. degree in July, 1989 and also learned Spanish.

He was enrolled in the Ph.D. program in Department of Physics, University of Florida, in August, 1989. Starting in 1990, he became interested in experimental low temperature physics and spent one year and half working in the Microkelvin Laboratory, Center for Ultralow Temperature Research, as a graduate research assistant. Then he began his research project in thermodynamic properties of solid ^3He under the supervision of Professor Dwight Adams. He accepted an offer beginning August, 1994 as a postdoctoral research associate at the Material Research Center, University of Puerto Rico, Rio Piedras.

I certify that I have read this study and that in my opinion it conforms to acceptable standards of scholarly presentation and is fully adequate, in scope and quality, as a dissertation for the degree of Doctor of Philosophy.



E. Dwight Adams, Chairman
Professor of Physics

I certify that I have read this study and that in my opinion it conforms to acceptable standards of scholarly presentation and is fully adequate, in scope and quality, as a dissertation for the degree of Doctor of Philosophy.



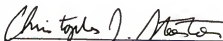
Gary G. Ihas, Cochair
Professor of Physics

I certify that I have read this study and that in my opinion it conforms to acceptable standards of scholarly presentation and is fully adequate, in scope and quality, as a dissertation for the degree of Doctor of Philosophy.

 for exam

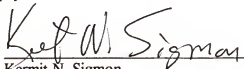
Neil S. Sullivan
Professor of Physics

I certify that I have read this study and that in my opinion it conforms to acceptable standards of scholarly presentation and is fully adequate, in scope and quality, as a dissertation for the degree of Doctor of Philosophy.



Christopher J. Stanton
Associate Professor of Physics

I certify that I have read this study and that in my opinion it conforms to acceptable standards of scholarly presentation and is fully adequate, in scope and quality, as a dissertation for the degree of Doctor of Philosophy.


Kermit N. Sigmon
Associate Professor of Mathematics

This dissertation was submitted to the Graduate Faculty of the Department of Physics in the College of Liberal Arts and Sciences and to the Graduate School and was accepted as partial fulfillment of the requirements for the degree of Doctor of Philosophy.

August 1994

Dean, Graduate School